

Mechanical feedback from stellar winds with an application to galaxy formation at high redshift

Yvonne A. Fichtner^{1*}, Luca Grassitelli¹, Emilio Romano-Díaz¹ and Cristiano Porciani¹

¹ *Argelander-Institut für Astronomie, Auf dem Hügel 71, D-53121 Bonn, Germany*

Accepted 2022 March 17. Received 2022 March 17; in original form 2022 January 15

ABSTRACT

We compute different sets of stellar evolutionary tracks in order to quantify the energy, mass, and metals yielded by massive main-sequence and post-main-sequence winds. Our aim is to investigate the impact of binary systems and of a metallicity-dependent distribution of initial rotational velocities on the feedback by stellar winds. We find significant changes compared to the commonly used non-rotating, single-star scenario. The largest differences are noticeable at low metallicity, where the mechanical-energy budget is substantially increased. So as to establish the maximal (i.e. obtained by neglecting dissipation in the near circumstellar environment) influence of winds on the early stages of galaxy formation, we use our new feedback estimates to simulate the formation and evolution of a sub- L_* galaxy at redshift 3 (hosted by a dark-matter halo with a mass of $1.8 \times 10^{11} M_\odot$) and compare the outcome with simulations in which only supernova (SN) feedback is considered. Accounting for the continuous energy injection by winds reduces the total stellar mass, the metal content, and the burstiness of the star-formation rate as well as of the outflowing gas mass. However, our numerical experiment suggests that the enhanced mechanical feedback from the winds of rotating and binary stars has a limited impact on the most relevant galactic properties compared to the non-rotating single-star scenario. Eventually, we look at the relative abundance between the metals entrained in winds and those ejected by SNe and find that it stays nearly constant within the simulated galaxy and its surrounding halo.

Key words: galaxies: evolution – galaxies: formation - galaxies: high-redshift - stars: winds, outflows

1 INTRODUCTION

Modern astrophysics relies on the inclusion of stellar-feedback processes in order to explain the low star-formation efficiency and baryon fraction observed in galaxies together with the metal enrichment of the circumgalactic and intergalactic media. The most commonly considered form of stellar feedback is the injection of mass, heavy elements, energy, and momentum by supernova (SN) explosions (e.g. Dekel & Silk 1986). The energy budget per unit mass of stars formed is dominated by core-collapse SNe (see e.g. fig. 10 in the review by Benson 2010). Each SN deposits 1-10 M_\odot of stellar ejecta initially moving at $\sim 10^4$ km s⁻¹ (much larger than the sound speed in the surrounding medium, thus leading to a blast wave) with a total kinetic energy of $\sim 10^{51}$ erg. The time evolution of the supernova remnant (SNR) produces a final momentum of a few $\times 10^5 M_\odot$ km s⁻¹, slightly depending on the properties of the environment (e.g. Kim & Ostriker 2015). The characteristic length scale of this phenomenon (say the radius of the dense shell that forms at the outer edge of the SNR between the Sedov-Taylor and the pressure-driven snowplow stages) ranges between a few and a few tens of pc determined by the ambient density. Multiple events clustered in space and time can build up superbubbles of hot gas in the interstellar medium (ISM) that break through the galactic disc and vent material into the halo (Norman & Ikeuchi 1989) or even beyond. It is widely believed that

SNe play a key role in the self-regulation of star formation within galaxies: gravity and cooling cause the gas to reach high densities and turn into stars thus producing feedback which drives some gas back to lower densities. Finally, SN explosions are thought to govern the small-scale structure of the ISM which comprises multiple ‘thermal phases’ in approximate pressure balance with one another. The ISM is often modelled as consisting of cold clouds (which dominate the mass budget) embedded in a hotter volume-filling inter-cloud medium. The physical conditions of the multi-phase ISM are determined by mass exchanges between the phases and the energy injection due to SNe (McKee & Ostriker 1977). In particular, the hot phase cools down slowly through the evaporation of the cold clouds.

Several lines of reasoning suggest that additional forms of stellar feedback should be included in galaxy-formation models (e.g. Hopkins et al. 2011; Brook et al. 2012; Stinson et al. 2012) although it is challenging to differentiate this need from the limitations of the sub-grid models for SN feedback and star formation (Rosdahl et al. 2017; Smith et al. 2019). Beyond SN explosions, there are several physical phenomena through which stellar feedback could affect the ISM, namely: proto-stellar jets, radiation pressure, photoionization, photo-electric heating, stellar winds and cosmic-ray acceleration at SNRs. These processes take place on rather small scales (ranging from a fraction of a pc to 10 pc) and can in principle play an important role in dispersing the gas after the onset of star formation. In particular, pre-SN or ‘early’ feedback is thought to strengthen the impact of the succeeding SN blast wave (e.g. Agertz et al. 2013;

* E-mail: yfichtner@astro.uni-bonn.de

Stinson et al. 2013; Geen et al. 2015; Hopkins et al. 2018) by removing gas from the birth giant molecular cloud (GMC). This scenario is supported by observations showing that gas is cleared out of the star-formation site before the first SN explosion (Barnes et al. 2020) and that GMCs are dispersed within 3 Myr after the emergence of unembedded high-mass stars (Chevance et al. 2022).

Due to computational cost, high-resolution simulations of stellar feedback within the ISM often concentrate on only one or two processes, namely individual and clustered SNe (Gatto et al. 2015; Iffrig & Hennebelle 2015; Kim & Ostriker 2015; Walch & Naab 2015; Girichidis et al. 2016; Körtgen et al. 2016), SNe and photoionization (Geen et al. 2016), SNe and stellar winds (Rogers & Pittard 2013; Gatto et al. 2017), photoionization (Dale & Bonnell 2011; Haid et al. 2019; Bending et al. 2020), photoionization and radiation pressure (Howard et al. 2016; Kim et al. 2016; Ali et al. 2018; Kim et al. 2018), photoionization and winds (Dale et al. 2014; Haid et al. 2018), radiation pressure (Skinner & Ostriker 2015), winds and radiation pressure (Silich & Tenorio-Tagle 2013). However, some recent simulations account for stellar winds, photoionization and SNe (Geen et al. 2015; Lucas et al. 2020; Rathjen et al. 2021). Stinson et al. (2013) developed an approximate numerical scheme to account for the collective effect of early stellar feedback in low-resolution simulations of galaxy formation. In this case, 10 per cent of the UV luminosity of a stellar population is injected as thermal energy before any SN events take place. Consequently, the gas immediately heats up to temperatures $T > 10^6$ K and then rapidly cools down to 10^4 K thus creating a lower density medium than in the absence of early feedback. This broadly mimics the formation of an H II region and effectively prevents star formation in the regions immediately surrounding young stellar clusters. On the other hand, Hopkins et al. (2011) developed a kinetic-feedback scheme to deposit the momentum imparted by radiation, SNe, and stellar winds in higher-resolution simulations. This is a sub-grid model which aims to describe physics taking place within GMCs and stellar clusters. This effort eventually led to the Feedback In Realistic Environments (FIRE) project (Hopkins et al. 2014) and its updated version FIRE-2 (Hopkins et al. 2018). In parallel, Agertz et al. (2013, see also Agertz & Kravtsov 2015) presented a sub-grid model for stellar feedback which takes into account the time-dependent injection of energy, momentum, mass and heavy elements from radiation pressure, stellar winds, SNe type II and Ia into the surrounding ISM. Undertaking a similar endeavour, Marinacci et al. (2019) presented the Stars and Multiphase Gas in GaLaxiEs (SMUGGLE) model which has been then combined with a radiative-transfer scheme in Kannan et al. (2019). Recent simulations of individual galaxies based on these schemes seem to self-consistently generate prominent galactic fountains and sustain inefficient (feedback-regulated) star formation for long time-scales, in agreement with observations (e.g. Hu et al. 2016; Wetzel et al. 2016; Hu et al. 2017; Li et al. 2017; Hopkins et al. 2018; Emerick et al. 2019; Lahén et al. 2019; Wheeler et al. 2019; Agertz et al. 2020; Emerick et al. 2020; Lahén et al. 2020; Li & Tonnesen 2020; Li et al. 2020; Gutcke et al. 2021).

In this work, we concentrate on the mechanical impact from stellar winds and neglect other forms of early feedback (e.g. radiative). Massive stars show radiation-driven outflows where material escapes the stellar surface with velocities of ~ 1000 km s⁻¹ and mass-loss rates of $\sim 10^{-6}$ M_⊙ yr⁻¹ (see Vink 2021, for a recent review). The energy injected into the ISM by winds over the lifetime of a massive star can be comparable to the mechanical energy of the subsequent SN explosion. Theoretical models and numerical simulations suggest that SN explosions should always take place within wind-blown cavities surrounded by dense shells (with radii > 10 pc) that have been seeded

with nuclear processed material (Tenorio-Tagle et al. 1990, 1991; Rozyczka et al. 1993; Smith & Rosen 2003; Dwarkadas 2005, 2007; Toalá & Arthur 2011; Geen et al. 2015). However, in stellar clusters, the fast stellar winds collide with each other and with the clumpy ISM producing shocks that heat the gas up. In this complex configuration, the wind energy can be lost via several channels (e.g. Rosen et al. 2014) and it is unclear whether stellar winds can drive the bulk motion of a cool, dense super shell surrounding the whole star-forming region. Recent simulations give contrasting answers. For instance, Rey-Raposo et al. (2017) find that winds act as an effective source of kinetic and thermal energy for the ISM while Lancaster et al. (2021) show that the bulk of the wind energy is lost due to turbulent mixing followed by radiative cooling. This loss, however, might be inhibited by magnetic fields (Rosen et al. 2021). What is certain is that the presence of a wind-driven bubble dramatically increases the fraction of SN energy which is retained by the ISM in the form of kinetic energy (Rogers & Pittard 2013; Fierlinger et al. 2016). In fact, the SN energy leaks through the chimneys (low-density regions) dug by the winds. On the other hand, studies that investigate the impact on to the ISM of ionising radiation from massive stars find a limited impact from stellar winds (e.g. Dale et al. 2014; Ngoumou et al. 2015; Geen et al. 2021). An important caveat worth mentioning here is that the various studies cited above adopt different approximations to model the small-scale structure of the ISM and therefore cannot be always directly compared.

Most simulations of galaxy formation (e.g. Agertz et al. 2013; Hopkins et al. 2018) rely on STARBURST99 (Leitherer et al. 1999; Vázquez & Leitherer 2005; Leitherer et al. 2010, 2014) to derive the mechanical input of winds from single stars. In order to bracket the distribution of rotation velocities in stellar populations, the latest version of STARBURST99 includes the Geneva 2012/13 stellar models with two rotation velocities (either zero or 40 per cent of the break-up velocity on the zero-age main-sequence) and two metallicity values. However, this is a rather limited set of evolutionary models covering a limited parameter range, which might not be fully representative of the rotational velocity distribution of stars and its metallicity-dependence.

We use the state-of-the-art open-source stellar-evolution code Modules for Experiments in Stellar Astrophysics (MESA, Paxton et al. 2011, 2013, 2015, 2018, 2019) in order to investigate a broader range of rotational velocities and metallicities. Moreover, since very massive stars have been observed in the Tarantula Nebula (e.g. Doran et al. 2013) in the Large Magellanic Cloud (LMC), we consider stellar models with initial masses up to nearly 160 M_⊙ (a factor of 1.3 larger than in STARBURST99). Finally, we account for the fact that the majority of stars are born in binary systems (Sana et al. 2012, 2013). The observational evidence for such large binary fraction led to a paradigm change in our understanding of stellar evolution. As one (or both) of the stars in a binary system fill their Roche lobes, a phase of mass transfer takes place. Material is exchanged between the companions through the first Lagrangian point or lost by the system. The outermost layers of the donor are stripped off and eventually accreted on to the secondary star. This significantly alters the masses and spectroscopic appearances of the stars and generates evolutionary sequences otherwise unattainable in a single-star scenario (e.g. De Marco & Izzard 2017), influencing the mass-loss and the rotation rates of stars. In some cases, the interaction and mass exchange can be unstable, leading to merger events. Although numerous uncertainties still exist regarding the modelling of binary systems, it is becoming increasingly clear that more realistic estimates of stellar feedback cannot ignore the impact of stellar multiplicity. This applies also to radiative feedback as interacting binaries enhance the production of

hydrogen- and helium-ionizing photons (e.g. Eldridge et al. 2017; Götberg et al. 2017) and harden the spectra of a stellar population (Götberg et al. 2019). Of particular interest are stripped helium stars, i.e. massive helium stars produced by binary interaction which emit the majority of their light at wavelengths shorter than the Lyman limit (Stanway et al. 2016; Götberg et al. 2019) on a time-scale beyond few Myr.

As a first sample application, we perform a series of zoom-in cosmological simulations following the formation of the central galaxy in a dark-matter (DM) halo of mass $M = 1.8 \times 10^{11} M_{\odot}$ at redshift $z = 3$. By considering different feedback models, we investigate the impact of stellar winds from rotating stellar models and binary systems on the resulting galaxy. We obtain objects with a stellar mass of a few $\times 10^9 M_{\odot}$ in line with those routinely observed in deep optical and infrared imaging surveys (see e.g. fig. 1 in Grazian et al. 2015). Note that, in the standard cosmological model, main-progenitor haloes of the selected mass at $z = 3$ end up, on average, within haloes with mass $M \simeq 10^{12} M_{\odot}$ at the present time (e.g. Wechsler et al. 2002). In this sense, our study is also relevant to Milky Way-like galaxies at $z = 0$.

The paper is structured as follows. In Section 2 (and in the appendices), we introduce our suite of stellar evolutionary models and derive the mechanical and chemical yields of stellar winds as a function of metallicity. In Section 3, we briefly review the implementations of stellar feedback in simulations and describe our own. The specifics of our cosmological simulations are given in Section 4 while, in Section 5, we study the properties of the simulated galaxies. Our main results and conclusions are listed in Section 6.

2 STELLAR EVOLUTION MODELS

We use the stellar evolution code MESA to compute different sets of models. For the mass-loss by stellar winds, we adopt the so-called ‘Dutch’ prescription based on Vink et al. (2001) for OB stars, Nugis & Lamers (2000) for the Wolf-Rayet (WR) regime, and de Jager et al. (1988) for late-type stars. For convection, we adopt the mixing-length theory (Böhm-Vitense 1958; Henyey et al. 1965) with a mixing-length parameter of 2 in the framework of the MLT++ scheme. This is motivated by the numerical difficulties commonly found in inflated stellar envelopes (Sanyal et al. 2015). For the overshooting, semi-convection, and thermohaline-mixing parameters, we assume the values of 0.345, 1, and 1, respectively (similar to Brott et al. 2011). Any remaining numerical parameters are set as in Marchant et al. (2016). We neglect magnetic fields.

2.1 Wind feedback from single stars

Our grid of models for single stars spans a mass range of $\log(M_{\text{ini}}/M_{\odot}) = 0.8\text{--}2.2$ in steps of $\log(M_{\text{ini}}/M_{\odot}) = 0.1$, where log is a short for \log_{10} . We consider eight different metallicities, namely 0.0001, 0.0004, 0.0007, 0.001, 0.002, 0.004, 0.008 and 0.02 and vary the initial surface rotation velocities, v_{ini} , between 0 and 600 km s^{-1} in intervals of 100 km s^{-1} . All our models are computed until core-helium exhaustion.

For a stellar model with mass M , radius R , luminosity L , surface hydrogen fraction X , metallicity Z , mass-loss rate \dot{M} , surface rotation velocity v_{rot} and critical rotation velocity v_{crit} (determined by MESA), we estimate the rate of kinetic energy ejected in the form of winds using (Leitherer et al. 1992; Puls et al. 2008)

$$\dot{E}_{\text{k}} = \frac{1}{2} \dot{M} v_{\infty}^2 \quad (1)$$

with the terminal wind velocity

$$v_{\infty} = d \sqrt{\frac{2GM}{R}} (1 - \Gamma_{\text{es}}) f_{\text{rot}} \left(\frac{Z}{0.02} \right)^{0.13}, \quad (2)$$

where d is the factor relating the terminal and escape velocities (2.6 for OB and 1.6 for classical Wolf-Rayet (cWR) and helium stars Abbott 1978; Gräfener & Vink 2013), Γ_{es} denotes the electron-scattering Eddington factor

$$\Gamma_{\text{es}} = \frac{0.2(1+X)L}{4\pi cGM}, \quad (3)$$

G is the gravitational constant, c the speed of light and

$$f_{\text{rot}} = \sqrt{1 - \left(\frac{v_{\text{rot}}}{v_{\text{crit}}} \right)^2} \quad (4)$$

(Puls et al. 2008).

Fig. 1 shows the kinetic energy E_{k} of the stellar wind integrated over the lifetime of the stellar models as a function of the initial mass M_{ini} for all the simulated rotation velocities and for $Z = 0.004$. As expected, E_{k} increases with M_{ini} . Stellar models with $M_{\text{ini}} \approx 100 M_{\odot}$ eject around 10^{51} erg, nearly three orders of magnitude more than stars with $M_{\text{ini}} \approx 8 M_{\odot}$. Stellar rotation leads to higher values of E_{k} . For instance, all the models with $v_{\text{ini}} = 600 \text{ km s}^{-1}$ and $M_{\text{ini}} > 40 M_{\odot}$ eject more than 10^{51} erg in stellar winds.

In Fig. 1, we use colours to highlight the relative contributions of different evolutionary stages¹ to E_{k} , namely OB dwarfs (OB), red supergiants (RSG), blue supergiant/luminous blue variables (BSG/LBV), WNL stars (WNL), helium stars (He-star) and cWR stars. The corresponding discussion of the mass yields is provided in Appendix A. For non-rotating models with $M_{\text{ini}} \lesssim 40 M_{\odot}$, a large fraction of the wind energy is ejected during the main-sequence, when the stellar model would appear spectroscopically as a OB dwarf, with terminal wind velocities of the order of 1000 km s^{-1} and mass-loss rates in the range $10^{-8}\text{--}10^{-5} M_{\odot} \text{ yr}^{-1}$ (Vink 2021). Stars in this mass range evolve past their main-sequence into red giants and supergiants. However, despite the relatively large mass-loss rates, the contribution from the post-main-sequence evolution accounts only up to around ~ 10 per cent of the total, due to the much slower winds of this phase (of about 10 km s^{-1} , de Jager et al. 1988; Smith 2014). On the other hand, stellar models with $M_{\text{ini}} > 40 M_{\odot}$ lose their H-rich envelope and evolve into cWR stars displaying dense and optically thick winds, with mass-loss rates of $\approx 10^{-5}\text{--}10^{-4} M_{\odot} \text{ yr}^{-1}$ and terminal velocities of $\approx 2000 \text{ km s}^{-1}$ (Nugis & Lamers 2000; Crowther 2007; Smith 2014). Although the WR phase lasts for ≈ 10 per cent of the stellar lifetime for models with $M_{\text{ini}} \approx 60 M_{\odot}$, it accounts for about half of E_{k} . At even higher masses ($M_{\text{ini}} \approx 100 M_{\odot}$), the WR phenomenon already occurs during the main-sequence evolution, i.e. the stellar models correspond to WNL (or WNH) stars (Crowther 2007; Smith 2014). The relative importance of the WR stage (starting $\approx 10^6$ yr after zero age) grows for $M_{\text{ini}} \gtrsim 40 M_{\odot}$.

¹ We differentiate between the evolutionary phases based on the position of the models in the Hertzsprung–Russell diagram (HRD) and the optical depth of their winds. We identify stellar models in the upper right corner of the HRD as BSG/LBV stars and cool (i.e. with effective temperature $T_{\text{eff}} \leq 10^4 \text{ K}$), lower luminosity stellar models as RSG. For the other types, we separate according to their position relative to the zero-age main sequence (ZAMS). Stellar models hotter than the ZAMS are either classified as helium stars or cWR stars, where cWR stars have optically thick winds (i.e. $\tau > 2/3$). Stellar models cooler than the ZAMS are either OB or WNL stars, where WNL stars have optically thick winds.

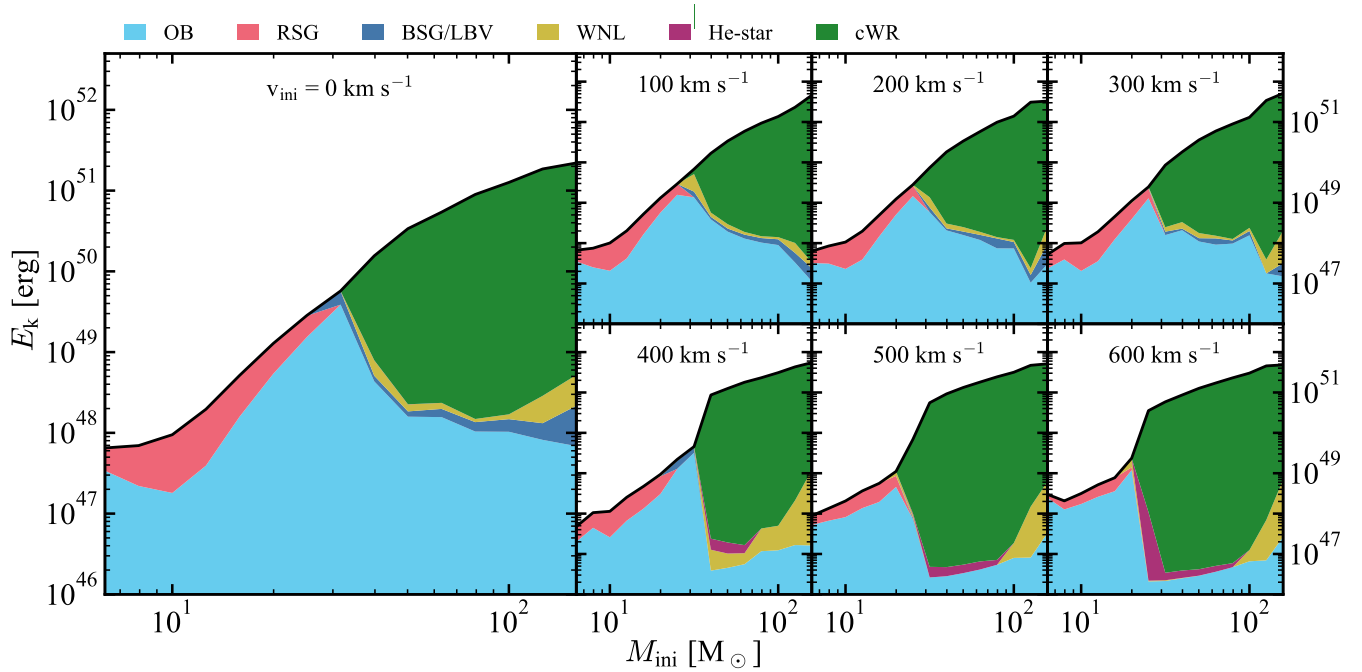


Figure 1. Total kinetic energy (black solid line) injected by winds into the ISM during the lifetime of a stellar model with initial mass M_{ini} and metallicity $Z = 0.004$. Different panels refer to different rotation velocities as indicated by the labels. In order to distinguish the relative contributions from different evolutionary stages (see footnote 1), we shade the area between the black curve and the bottom axis using different colours. The vertical extent of each colour indicates the fraction of energy released during each phase using a linear scale (e.g. a contribution of 50 per cent covers half of the distance between the bottom axis and the black curve).

while the blue supergiants (including a potential LBV phase) only contribute a few per cent of the total mechanical yield.

Rotation makes stellar cores larger while reducing the extent of the H-rich envelopes thus producing more massive post-main-sequence helium/WR stars. In consequence, both the WR contribution and E_k increase at fixed initial mass (especially for $M_{\text{ini}} \approx 40\text{--}50 M_{\odot}$). Mass-loss rates are also enhanced although with lower terminal velocities.

2.2 Wind feedback from binary stars

It is well known that most stars form in binary systems (e.g. Sana et al. 2012) and this dramatically affects their evolutionary path (Podsiadlowski et al. 1992; Van Bever & Vanbeveren 2000; de Mink et al. 2013; Mandel & de Mink 2016; Marchant et al. 2016; Langer et al. 2020). However, many aspects ranging from the way stars in binaries interact (including common-envelope phases Paczynski 1976; Ivanova et al. 2013) to the intrinsic fraction of binary systems at different metallicities are still poorly understood. None the less, we attempt to investigate the impact of binaries to the expected mechanical and chemical feedback by stellar winds of stellar populations.

We compute binary stellar models with different metallicities (0.0001, 0.0004, 0.0008, 0.004, 0.008 and 0.02). For simplicity, we assume a fixed binary mass ratio of 0.6 and cover the same initial-mass range for the primary star as we did for single stars, although this time we use steps of $\log(M_{\text{ini}}/M_{\odot}) = 0.2$. We consider four different values for the orbital period, namely $P = 10^{0.6}, 10^1, 10^2$ and 10^3 days. Finally, we take into account the fact that, in binary systems, some of the kinetic energy of the stellar winds is dissipated due to the interaction between the winds generated by the primary

and secondary stars (Usov 1991; Stevens et al. 1992). We base our estimate on the momentum balance between the stellar winds by adopting the reduction factor

$$f_{\text{ww}} = \begin{cases} 1 - \frac{\pi^2}{16} \sqrt{\frac{M_s v_{\text{inf},s}}{M_p v_{\text{inf},p}}} & \text{for } \dot{M}_p v_{\text{inf},p} > \dot{M}_s v_{\text{inf},s}, \\ 1 - \frac{\pi^2}{16} \sqrt{\frac{M_p v_{\text{inf},p}}{M_s v_{\text{inf},s}}} & \text{otherwise,} \end{cases} \quad (5)$$

(De Becker & Raucq 2013) where the indices p and s refer to the primary and secondary star, respectively. The maximum attenuation ($f_{\text{ww}} = 0.38$) is obtained when the two stars produce winds with equal momenta.

Once the primary star reaches core-helium exhaustion, we follow the remaining evolution of the secondary as if it was a single star. In small corners of the investigated parameter space, our evolutionary models suggest that a merger of the companions should take place, and the calculation is inevitably stopped as, presently, no stellar-evolution code is able to model such merger events (see however Glebbeek et al. 2013; Schneider et al. 2016). In these cases, we interpolate through our grid of models.

In Fig. 2, we show E_k as a function of M_{ini} for the primary and secondary models. Barring the most massive stars, both the primaries and the secondaries return more kinetic energy via their stellar winds compared to the single non-rotating case. The largest contribution to E_k comes from helium and WR stars. In fact, all the binary models experience mass-transfer and the primaries lose their outer H-rich envelope. They thus achieve effective temperatures of about $5 \times 10^4\text{--}10^5$ K, becoming either stripped He-stars with optically thin winds or cWR stars, with much larger terminal wind velocities than late-type stellar models. The mass-gainers secondary models also show larger

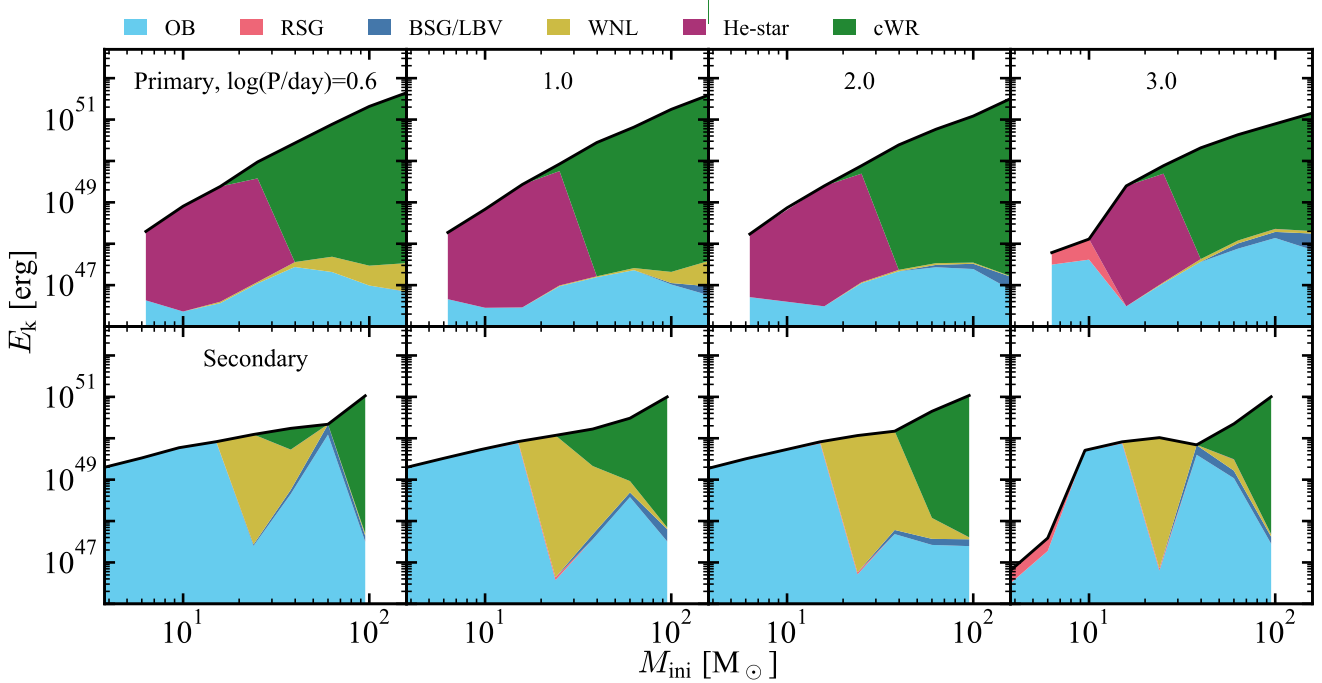


Figure 2. As in Fig. 1 but for binary systems with a fixed mass ratio of 0.6 and different periods (indicated by the labels).

E_k compared to single star models of the same mass, particularly for the lowest considered initial mass and the short periods (i.e. those undergoing mass-transfer during the main-sequence phase). The reason is twofold: mass accretion on to the secondary models leads to higher masses and luminosities compared to the single star case, and a significant fraction of the mass stripped from the primary component of the binary systems is not accreted and leaves as stellar wind of the secondary model during its OB phase (given that mass-transfer takes place almost always during the main-sequence phase of the secondary stellar models), contributing to the kinetic stellar feedback (see also Appendix A).

2.3 Feedback from a stellar population

In order to model the energy injection into the ISM by a simple coeval population of single stars, we use the parametrization for the initial mass function (IMF) introduced by Kroupa (2001). We consider stars within the mass range $10^{-1} \leq M \leq 10^{2.2} M_\odot$ and account for the SN explosion and stellar winds of the models with $M > 10^{0.9} M_\odot$ but we assume that stars with $M > 40 M_\odot$ collapse directly to a black hole at the end of their lifetime without releasing energy into the ISM.

For consistency with previous work, we associate an energy of 10^{51} erg to every SN explosion (e.g. Scannapieco et al. 2012; Agertz et al. 2013; Crain et al. 2015), although this simplification does not account for the variety of SNe seen in nature. We make sure that this energy is released into the ISM when a massive star reaches the end of its lifetime (i.e. the injection time is different for each stellar model). We estimate the ejected mass by computing the difference between the final mass of the stellar model and the average remnant mass derived in Sukhbold et al. (2016).

We consider three cases. In the first one, we only use single non-rotating stellar models while, in the second one, we combine sin-

gle rotating models according to an empirically derived distribution of initial rotation velocities which depends on metallicity (see Appendix B). Finally, our third option also accounts for binary stars. In this case, we assume that 70 per cent of the stellar mass is in binary systems and that the remaining 30 per cent is contributed by single stars. For the binaries, we apply the Kroupa IMF to the mean mass in each system and assume a flat orbital-period distribution in log-space (between $\log(P/\text{day}) = 0.3$ and 3.3) across all considered metallicities. This is consistent with observations in both the Galaxy and the LMC (Kobulnicky et al. 2014; Almeida et al. 2017).

Fig. 3 shows the time dependence of the cumulative kinetic energy ejected by one solar mass of coeval stellar evolutionary models (with $Z = 0.004$) in the form of winds (see Appendix A for the corresponding discussion of the mass yields). The top panel refers to single rotating stellar models while binary systems are considered in the bottom one. In the first 2.5 Myr, a few $\times 10^{47}$ erg M_\odot^{-1} are ejected by stellar models in the OB stage. Subsequently, the most massive stellar models reach the WR phase, leading to a steep increase in the total energy ejected. Overall, the cWR stage contributes nearly 60 per cent of the total ejected energy (although only the most massive stars experience it). For single stars (binaries), 90 (65) per cent of the wind energy is ejected before the onset of the first SN explosion, which takes place when the stellar population has an age of 5 Myr. It is worth mentioning that the binary systems show more prominent contributions from the post-main-sequence helium star models. For instance, stripped helium stars originating from binary interactions start playing a relevant role after 10 Myr and provide roughly 10 per cent of the total energy.

So far we have only discussed the stellar models with $Z = 0.004$. In Fig. 4, we present the metallicity dependence of the kinetic energy (E_p , top panel), mass (M_p , middle panel), and metals ($M_{Z,p}$, bottom panel) ejected from a coeval population per unit stellar mass. Single non-rotating stars show the strongest metallicity dependence of E_p

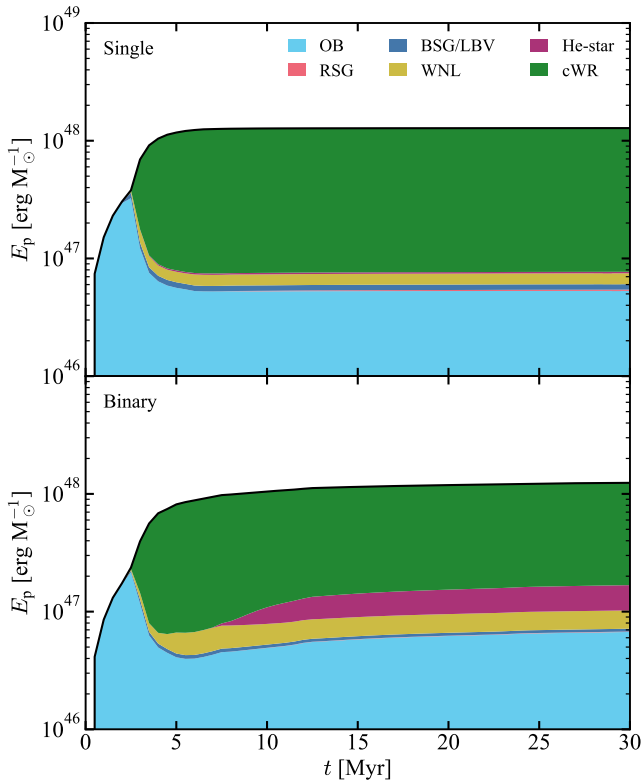


Figure 3. Cumulative kinetic energy ejected in the form of winds by a coeval simple stellar population with metallicity $Z = 0.004$. Plotted is the energy per unit stellar mass as a function of the population age. The top and bottom panels refer to populations of single and binary stars, respectively. Colour shading is as in Fig. 1.

and $M_{Z,p}$ while the inclusion of rotating and binary stars leads to a remarkably shallower relation. The reason is twofold: (i) the probability density function of the initial rotational velocity peaks at higher velocities with decreasing Z (thus driving larger rates of mass-loss by stellar winds) and (ii) binary interaction leads to the formation of stripped helium and WR stars also when envelope self-stripping by stellar winds is not sufficient, i.e. at low Z . Note that, at low metallicity, single non-rotating stars eject nearly one order of magnitude less energy and three orders of magnitude less metals than a more realistic population composed of a mix of rotating and binary stars. This difference could play an important role in modelling the early phases of galaxy formation. Regarding the integrated mass-loss quantified by M_p , we note that all model populations show a similar metallicity dependence although with systematically higher mass yields from the rotating and binary models, by approximately a factor two.

We compare our results for a coeval stellar population including a combination of binary systems and rotating single stars with the results from STARBURST99, which are derived adopting the Geneva evolutionary tracks for single stars. We use the same IMF but the most massive model in the Geneva set ($120 M_\odot$) is lower than in our set. For the non-rotating single stars, the ejected energy per unit stellar mass we derive is consistent with that from STARBURST99, with an approximate metallicity dependence of $E_p \propto Z$. On the other hand, the mix of binary systems and rotating single-star models shows a shallower relation with $E_p \propto Z^{0.65}$.

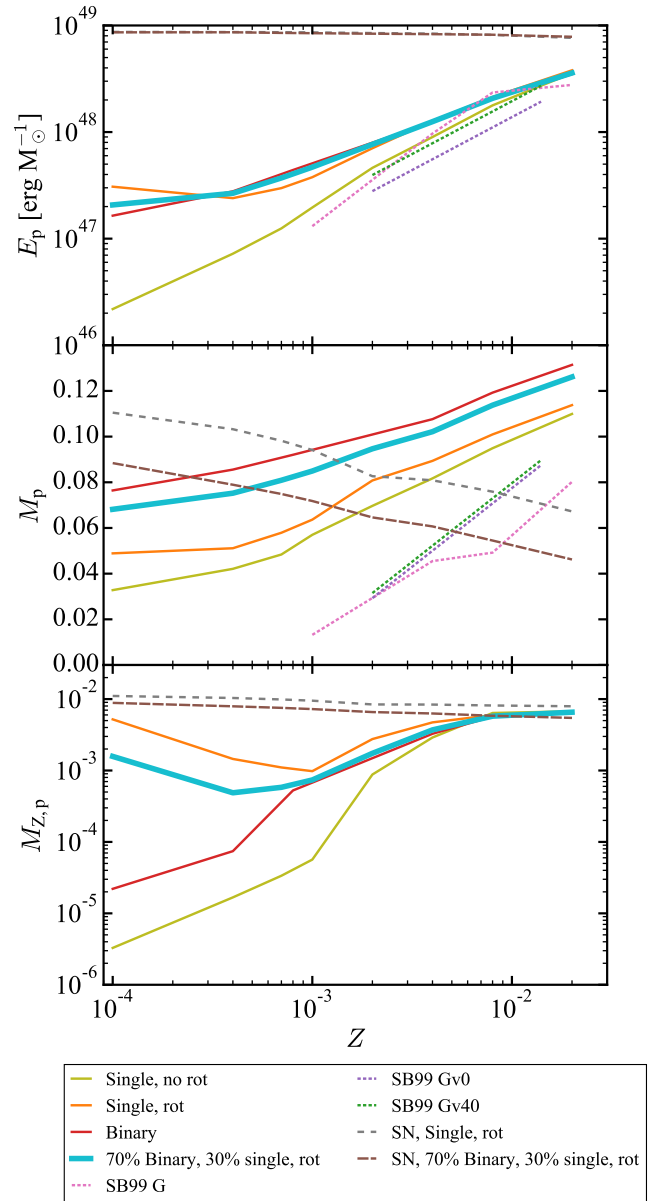


Figure 4. Mechanical and chemical yields of winds emitted by different stellar populations (see labels) within the first 30 Myr as a function of absolute metallicity. From top to bottom in the panels, we show the (time-integrated) ejected energy per unit stellar mass, the ejected mass fraction and the corresponding metal fraction. For comparison, the corresponding yields of SNe are shown with dashed lines (assuming the metal yield is 10 per cent). Also shown are the yields of three different tracks from STARBURST99: Geneva standard (SB99 G, Schaller et al. 1992), v00 (SB99 Gv0, Ekström et al. 2012, tracks with $v_{\text{ini}} = 0$) and v40 (SB99 Gv40, Ekström et al. 2012, tracks with $v_{\text{ini}} = 0.4 v_{\text{crit}}$).

2.4 Discussion and a caveat

Stars inject kinetic energy and mass into the surrounding medium during their whole lifetime. However, a fraction of this energy is likely dissipated in the nearby circumstellar regions (e.g., Garcia-Segura et al. 1996a,b) due to the variable wind velocity over the evolution of a single star (Vink et al. 2001). For instance, the slow and dense RSG or LBV outflows swept by the faster wind during the

following WR phase can lead to a significant fraction of the kinetic energy being lost at scales smaller than the minimum resolution of our simulations of galaxy formation (~ 40 pc, see Section 4). Moreover, in a stellar cluster, some energy will be also dissipated in the shocks forming between colliding stellar winds and between the winds and the clumpy ISM. As mentioned in the introduction, different authors reach opposite conclusions regarding the entity of the dissipation (Rey-Raposo et al. 2017; Lancaster et al. 2021; Rosen et al. 2021). In the absence of a consensus, in this work, we inject the whole energy released by the winds and SNe into the ISM and solve the equations of fluid dynamics to determine gas flows on scales of tens of pc. In this sense, our study quantifies the maximum effect that could be possibly driven by stellar winds.

It is also important to stress that, despite the large observational and theoretical efforts, mass-loss prescriptions in stellar models are still uncertain² by about a factor of three at Galactic metallicity (Smith 2014; Vink 2021, and references therein). Uncertainties are even more severe at lower metallicities, where the lack of observational constrains and the low abundance of the metals that are responsible of the radiatively driven stellar wind do not allow for fully reliable estimates. This is particularly the case for the cWR stars which, as shown in Fig. 1 produce a large amount of mechanical feedback. These uncertainties present a major challenge in determining the energy and momentum budget that a stellar population injects into the ISM in the form of winds.

3 SIMULATING STELLAR FEEDBACK

3.1 The state of the art

Different methods have been used to include SN feedback in numerical hydrodynamic simulations of galaxy formation. In cosmological runs that cover large volumes and achieve a spatial resolution of ≈ 0.2 –1 kpc (insufficient to reveal individual SNRs and the complex multi-phase structure of the ISM), SN feedback was originally implemented as a single injection of thermal energy and mass from a simple stellar population. It turns out, however, that the energy is deposited in too large a volume or mass. Consequently, the bulk of the injected energy is immediately radiated away (without having much mechanical impact on the ISM) due to the high densities of the star-forming regions (e.g. Katz 1992). In order to prevent this ‘overcooling problem’ some ad hoc shortcuts have been adopted. One possibility is to artificially prevent the heated gas from cooling for a time comparable with the local dynamical time-scale (~ 30 Myr) so that to convert part of the deposited energy into actual gas kinetic energy and mimic the production of hot bubbles (possibly driving outflows) generated by the combination of blast waves from multiple SN explosions (Gerritsen 1997; Gerritsen & Icke 1997; Thacker & Couchman 2000; Sommer-Larsen et al. 2003; Kereš et al. 2005; Stinson et al. 2006; Governato et al. 2007). The rationale behind this method is that the volume-filling cavities of low-density gas in the multi-phase ISM are not resolved and thus radiative losses are overestimated in the simulations. Alternatively, one can implement a ‘kinetic feedback’ scheme in which the gas elements are imparted some outwardly directed momentum (and are decoupled from hydrodynamic forces until they leave the galaxy) to simulate the launching of a galactic wind (e.g. Navarro & White 1993; Mihos & Hernquist

1994; Springel & Hernquist 2003; Oppenheimer et al. 2010; Vogelsberger et al. 2013; Davé et al. 2017; Valentini et al. 2017; Pillepich et al. 2018). This can be implemented in many different ways and generally requires the introduction of free parameters. Dubois & Teyssier (2008, see also Mori et al. 1997, Gnedin 1998), for instance, impose around each SN event a spherical Sedov blast-wave profile for density, momentum and total energy, with a radius equal to a fixed physical scale resolved with a few computational elements. This radius should approximately match the size of super-bubbles blown by multiple clustered SN explosions (hundreds of pc) and is obviously much larger than individual SNRs. Note that this radius also sets the injection scale for turbulence in the simulated ISM. Kinetic feedback schemes, however, do not properly account for the thermal state of the ISM as they neglect the hot phase produced by SNe. Approximate sub-grid models are thus used to determine the ‘effective pressure’ of the multi-phase ISM as a function of the coarse-grained density of the gas in the simulations (Yepes et al. 1997; Hultman & Pharasyn 1999; Springel & Hernquist 2003; Schaye & Dalla Vecchia 2008; Murante et al. 2010). Basically, the use of an effective equation of state prevents the dense gas from cooling down to arbitrarily small temperatures and artificially fragmenting.

On the opposite extreme, non-cosmological simulations of either an idealized ISM or individual molecular clouds and parts of disc galaxies have investigated the impact of individual SNe on their surroundings with sub-pc spatial resolution (e.g. Thornton et al. 1998; Creasey et al. 2013; Gatto et al. 2015; Iffrig & Hennebelle 2015; Kim & Ostriker 2015; Walch & Naab 2015; Walch et al. 2015; Girichidis et al. 2016; Simpson et al. 2016; Kim & Ostriker 2017; Hirai et al. 2021; Smith et al. 2021). The emerging picture is that most of the energy injected by a SN into the ISM is rapidly thermalised and radiated away. However, a fraction ranging between a few to ten per cent is later found as kinetic energy of the ambient medium, with some dependence on the local density and the time at which the retained energy is estimated.

In the last decade or so, it has become computationally feasible to simulate individual galaxies with a spatial resolution of a few tens of pc which partially reveals the turbulent and multi-phase structure of the ISM. At this resolution, the largest sites of star formation (where giant molecular clouds come into existence) can be localised in the simulations although their internal structure cannot be probed. Ceverino & Klypin (2009) showed that, with a spatial resolution of ~ 50 pc, it is possible to drive galactic winds without artificially delaying gas cooling after injecting SN energy. This, however, requires that some SNe explode outside of the dense regions in which they formed due to OB-runaway stars. Several studies devised an optimal strategy for simulating SNR and deal with the overcooling problem (Kim & Ostriker 2015; Martizzi et al. 2015, but see also Hopkins et al. 2014 and Kimm & Cen 2014). If the radius of the shell forming at the end of the Sedov-Taylor stage (which is sometimes called the cooling radius) is resolved with a sufficient number of elements (~ 10), then one should inject 10^{51} erg of thermal energy and let the hydrodynamic solver track the buildup of momentum. Otherwise, if the ambient density is too high for the achieved resolution (and thus the shell radius too small), one should directly inject the full momentum generated during the Sedov-Taylor phase. The latter approximation fails to catch the impact of the hot gas (and, possibly, underestimates galactic winds) but anyway drives turbulence in the warm and cold phases of the ISM and allows for self-regulated star formation.

² This is mostly due to the presence of inhomogeneities, called clumping, that affect the line diagnostics (Moffat et al. 1988; Puls et al. 2008; Sundqvist & Owocki 2013).

3.2 Our implementation

We adopt two different numerical schemes to simulate SN feedback. In the first one (dubbed T as a short for ‘thermal feedback’), the mass, metals and energy ejected by SNe are deposited at the location of stellar particles with age t_{SN} . The SN energy is used to alter the thermal budget of the surrounding ISM and gas cooling is switched off as in the standard RAMSES implementation with a characteristic time-scale of 20 Myr.

In the second scheme (dubbed M as a short for ‘mixed thermal-kinetic feedback’), the ejecta are distributed within a sphere of radius $r_{\text{Sed}} = 150$ pc and the SN energy is partitioned between the thermal energy of the gas (corresponding to 70 per cent of the total) and a kinetic term accounting for the bulk motion of the ISM within r_{Sed} (Dubois & Teyssier 2008). Mass, momentum and kinetic energy are distributed within r_{Sed} as in a spherically-symmetric Sedov blast wave. We assume a unitary mass-loading factor, i.e. that the gas mass entrained by the SN explosion is equal to that of the stellar particle. Delayed cooling is implemented as in the T model.

We use the blast-wave model also to describe the combined effect of stellar winds and SNe. In this case, however, mass, energy and momentum are continuously injected into the ISM by young stellar particles. The corresponding rates are obtained by interpolating the tables we derived in Section 2.

4 NUMERICAL METHODS

As a first sample application of our stellar models to the field of galaxy formation and evolution, we investigate the impact of stellar winds on the structure of a high-redshift galaxy. To this end, we use the adaptive-mesh-refinement (AMR) code RAMSES (Teyssier 2002) to perform several cosmological zoom-in simulations of a sub- L_* galaxy at $z = 3$. Each simulation starts from the same initial conditions (IC) but adopts different feedback models.

4.1 Initial conditions and refinement strategy

We consider a flat Lambda cold dark matter cosmological model (Planck Collaboration VI 2020) and simulate the formation of a galaxy within a cubic periodic box of comoving side $L_{\text{box}} = 6 h^{-1}$ Mpc. Initial conditions (IC) are generated at $z = 99$ with the MUSIC code (Hahn & Abel 2011). We set up zoom-in simulations following a multistep procedure. We first generate IC with a uniform resolution using $2^{l_{\text{ini}}}$ elements along each spatial dimension (with $l_{\text{ini}} = 7$) and run a DM-only simulation until $z = 3$. After identifying haloes with the AMIGA HALO FINDER code (AHF, Gill et al. 2004; Knollmann & Knebe 2009), we pick a halo with a virial mass of $M_{\text{vir}} \sim 10^{11} M_{\odot}$ and a relatively quiescent late mass-accretion history (the virial radius R_{vir} encloses a mean density of $200 \rho_{\text{crit}}$, with ρ_{crit} being the critical density for closure of the Universe). At this point, we use the zoom-in technique to re-simulate the selected halo at higher spatial resolution. In brief, all the simulation particles found within $3R_{\text{vir}}$ from the halo centre at $z = 3$ are traced back to the IC and the corresponding volume is resampled at a higher resolution. The final configuration includes several nested levels with different spatial resolutions.

We investigate discreteness effects and numerical convergence (see Sections 5.1 and 5.2) by generating ICs with two different maximum levels of refinement ($l_{\text{ini}} = 9$ and 10) corresponding to different mass resolutions for the DM component ($m_{\text{DM}} = 1.8 \times 10^5$ and 2.2×10^4

Table 1. Main properties of the simulation suite.

Name	Feedback	t_{SN} Myr	Winds	$l_{\text{ini}}/l_{\text{max}}$	Δx pc	n_{\star} cm^{-3}
S9T	Thermal	10	No	9/15	68	10
S9M	Mixed	10	No	9/15	68	10
E9S	Mixed	Variable	No	9/15	68	10
E9O	Mixed	Variable	Non-rot	9/15	68	10
E9R	Mixed	Variable	Rot	9/15	68	10
E9B	Mixed	Variable	Rot+Bin	9/15	68	10
S10M	Mixed	10	No	10/16	34	20
E10R	Mixed	Variable	Rot	10/16	34	20
E10B	Mixed	Variable	Rot+Bin	10/16	34	20

M_{\odot} , respectively). In the remainder of this paper, we refer to the simulations obtained in the two cases as ‘low-’ and ‘high-resolution’.

During run time, the AMR technique refines (and coarsens) the grid structure used to solve the fluid equations for the gas and the Poisson equation for the gravitational potential based on pre-determined criteria. We adopt a quasi-Lagrangian scheme which is uniquely based on mass density. A cell is split if it contains more than eight DM particles or a total baryonic mass (stars and gas) corresponding to the same density contrast. In order to prevent runaway refinement early on, triggering a new level is only allowed after the simulation has reached a specific cosmic time so that to match the refinement strategy of the corresponding DM-only case (which we always run first). This strategy makes sure that the resolution of the grid in physical units remains nearly constant (in a stepwise sense). For all simulations, the AMR algorithm adds six levels of refinement until $z = 3$, corresponding to a nominal spatial resolution of 68 and 34 physical pc for the low- and high-resolution simulations, respectively.

In order to facilitate the interpretation of the results, we save snapshots every 5 Myr for the simulations with $l_{\text{ini}} = 10$ (10 Myr for those with $l_{\text{ini}} = 9$).

4.2 Gas physics and star formation

For the gas, we assume an equation of state with polytropic index $\gamma = 5/3$. In order to avoid spurious fragmentation, we artificially add thermal pressure where needed in order to resolve the Jeans length with four grid elements or more (Truelove et al. 1997; Teyssier et al. 2010). The gas is ionised and heated up by the default time-dependent uniform cosmic UV background in RAMSES which is exponentially suppressed where the physical number density of gas particles, n , exceeds 0.01 cm^{-3} to approximate self-shielding (e.g. Tajiri & Umemura 1998). Our runs include gas cooling from H, He and metals.

The conversion of ‘cold’ and dense gas into stars is modelled with a Poisson process in which the average follows the relation (Schmidt 1959)

$$\dot{\rho}_{\star} = \frac{\epsilon_{\star}}{t_{\text{ff}}} \rho_{\text{gas}}, \quad \text{if } T < 2 \times 10^4 \text{ K and } n > n_{\star}, \quad (6)$$

which relates the star-formation-rate (SFR) density $\dot{\rho}_{\star}$ and the gas density ρ_{gas} in terms of the star-formation efficiency $\epsilon_{\star} = 0.01$ and the free-fall time of the gas $t_{\text{ff}} = \sqrt{3\pi/(32G\rho_{\text{gas}})}$ (e.g. Agertz et al. 2011; Perret et al. 2014; Kretschmer & Teyssier 2020). We set the density threshold for star formation to $n_{\star} = 10$ and 20 cm^{-3} in the low- and high-resolution simulations, respectively. Stellar particles have a mass of $2.5 \times 10^4 M_{\odot}$ in the high-resolution runs which is large enough to properly sample the IMF also for massive stars.

4.3 Stellar feedback

We consider two sets of simulations. Namely, those adopting a standard SN feedback model (name starting with S) and those based on our stellar tracks (name starting with E, short for early feedback). Each stellar particle in the simulations represents a coeval stellar population. In the standard feedback model, we consider type II SNe originating from these populations. A single occurrence takes place $t_{\text{SN}} = 10$ Myr (Agertz et al. 2011; Ocvirk et al. 2020) after the birth of the stellar particle. The total ejected mass and energy by SNe from a stellar population with mass M_{pop} are $M_{\text{ej}} = 0.1 M_{\text{pop}}$ and $E_{\text{ej}} = (M_{\text{ej}}/10 M_{\odot}) 10^{51}$ erg (Dubois & Teyssier 2008; Agertz et al. 2011; Ocvirk et al. 2020) which is equivalent to assuming that every SN event injects (on average) 10^{51} erg and $10 M_{\odot}$ into the ISM. The corresponding metal yield is 10 per cent (see equation 4 in Perret et al. 2014).

In the E-simulations, instead, SN events do not all take place after 10 Myr after the birth of a stellar particle. On the contrary, mass, metals and energy are injected into the ISM at all times reflecting the lifetime of the stellar models presented in Section 2 and the IMF by Kroupa (2001). In this case, the masses ejected by SNe are obtained from the stellar tracks (see Section 2.3) while we still assume that each SN event releases 10^{51} erg and that the metal yield is 10 per cent. In addition, the contribution generated by stellar winds is also taken into account.

A list of all simulations and their distinguishing features are presented in Table 1. The naming convention is as follows: as previously mentioned, the first letter (S or E) indicates whether a standard SN-only model or the more-sophisticated early-feedback scheme is used. This is followed by a number which gives the maximum level of refinement in the IC (9 or 10). Finally, the last letter gives further details about the adopted feedback model. For the S simulations, T and M stand for thermal feedback and mixed thermal-kinetic feedback, respectively. On the other hand, for the E simulations (which all use the blast-wave model) there are four possibilities. The letter S indicates that only SN feedback is considered while the letters O, R and B refer to SNe and winds from non-rotating single stars, rotating single stars, and a mix of rotating single stars and binaries, respectively.

5 RESULTS

We now present the results of the simulations. In what follows, we assume a solar metallicity of 2 per cent by mass (i.e. $Z_{\odot} = 0.02$) and all distances are given in physical units unless explicitly stated otherwise.

The virial mass and radius of the re-simulated DM halo at $z = 3$ are nearly the same in all simulations, namely $M_{\text{vir}} = 1.8 \times 10^{11} M_{\odot}$ and $R_{\text{vir}} = 43$ kpc. We conventionally define the central galaxy as the collection of gas and stars enclosed within a radius of $R_{\text{gal}} = 0.1 R_{\text{vir}}$ and located at the centre of the DM halo (e.g. Scannapieco et al. 2012). In order to give a visual impression of the environment surrounding the galaxy, in Fig. 5, we show a projected map of the gas density for the run E10B at $z = 3$. The top panel has a side length of 400 kpc and illustrates the area of the intergalactic medium in which the DM halo resides while the bottom panel zooms in the central region (here, R_{vir} and R_{gal} are highlighted with a grey and a black circle, respectively). The intricate habitat of the galaxy within R_{vir} is characterised by a nearly planar gas distribution veined with dense filaments feeding the central object and its multiple compan-

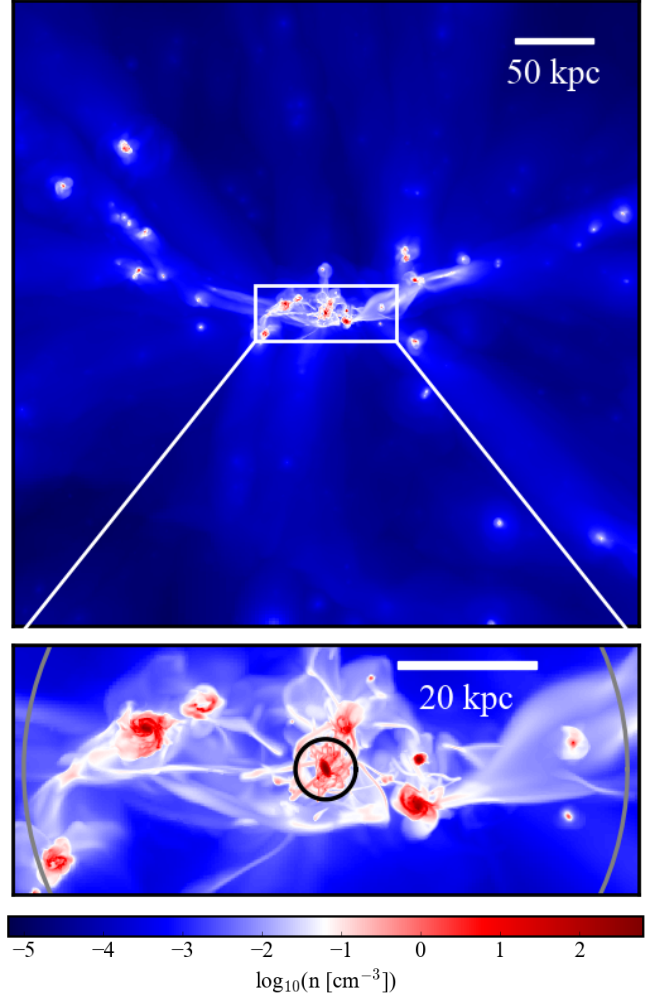


Figure 5. Projected map of the gas distribution in the E10B run at $z = 3$. Each pixel is colour coded according to the maximum density along the line of sight within a cube of side length 400 kpc. In the bottom zoomed-in panel, the halo and the galaxy radii are indicated with a grey and a black circle, respectively.

ions (which, in all probability, will eventually merge with the main galaxy).

5.1 Global properties and morphology

The main properties of the simulated galaxies at $z = 3$ are listed in Table 2. These include the stellar mass (M_*), the gas mass (M_{gas}), the average SFR over the past 200 Myr as well as the mass-weighted mean metallicity of the stars (Z_{star}) and of the gas (Z_{gas}), both in solar units.

As a first step, we compare the different SN-only runs. Looking at the low-resolutions simulations reveals that the thermal feedback scheme (S9T) is rather inefficient as it produces nearly three times larger M_* , Z_{star} and Z_{gas} than those obtained considering the two mixed schemes based on the blast-wave model (S9M and E9S). On the other hand, considering that massive stars have different lifetimes (E9S) causes a 20 per cent reduction in M_* and Z_{star} with respect to S9M.

Accounting for stellar winds substantially reduces M_* , the SFR

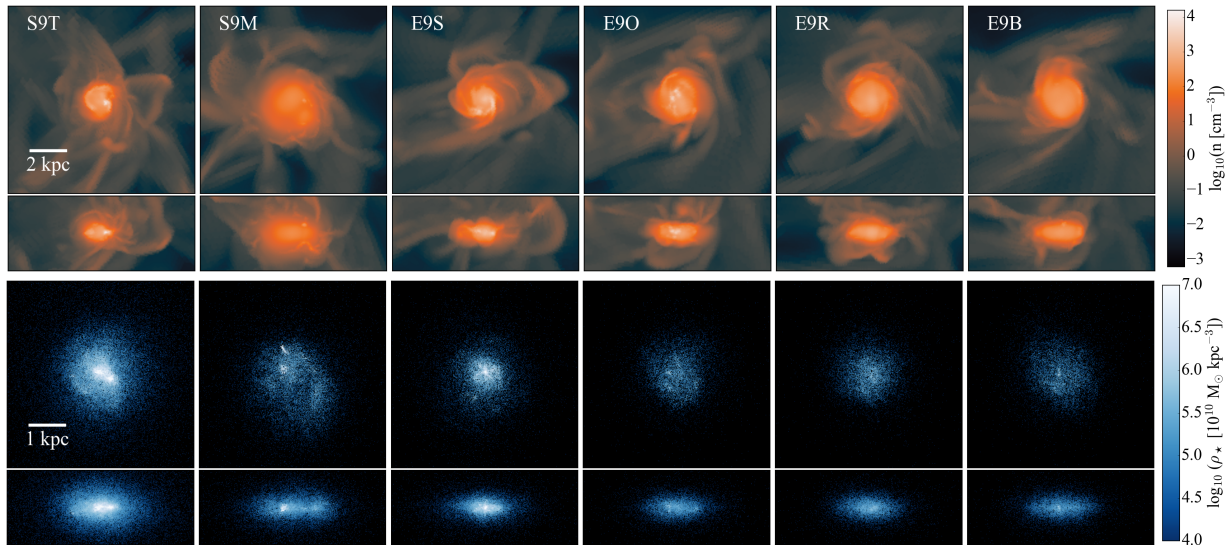


Figure 6. Face-on and edge-on false-colour images of the gas (top row) and stellar (bottom row) distributions in the low-resolutions simulations at $z = 3$. Shown are the maximum gas density along the line of sight and the star volume density at the location of the stellar particles. Note the different length scales used for gas and stars as indicated by the white yardsticks.

Table 2. Properties of the simulated galaxies at $z = 3$.

Name	M_{\star} $10^9 M_{\odot}$	M_{gas} $10^{10} M_{\odot}$	SFR $M_{\odot} \text{ yr}^{-1}$	Z_{star} Z_{\odot}	Z_{gas} Z_{\odot}
S9T	5.84	0.93	9.34	0.169	0.248
S9M	2.40	1.37	4.02	0.058	0.092
E9S	1.90	1.41	3.17	0.047	0.065
E9O	0.96	1.47	1.38	0.030	0.043
E9R	0.97	1.49	1.32	0.033	0.046
E9B	0.97	1.47	1.31	0.022	0.031
S10M	3.80	1.25	5.11	0.087	0.142
E10R	1.09	1.59	1.48	0.034	0.049
E10B	1.16	1.55	1.49	0.024	0.035

and the metallicities (all by at least a factor ranging between 2 and 3.5) while it does not leave an imprint in M_{gas} . In fact, it is to be expected that winds make stellar feedback more efficient (i) by injecting non-negligible amounts of energy and momentum into the ISM and (ii) by lowering the gas density around stellar particles before SN explosions take place. However, the different stellar-wind models (O, R, B) appear to generate galaxies with very similar global properties although accounting for rotation and binaries substantially increases the instantaneous energy injection rate. This unexpected behaviour arises from the fact that the winds of single non-rotating stars already provide enough energy early on to raise the gas temperature in the simulations above the threshold at which star formation is inhibited (Stinson et al. 2013) – see equation (6). Due to this threshold effect, the SFR of the galaxies does not change much when additional energy is injected by rotating and binary stars. Basically, when winds are accounted for, the formation of stellar particles in the spatial and temporal proximity of recently born ones is reduced considerably with respect to the simulations that only consider SN feedback.

Another thing worth mentioning is that the O, R and B wind models generate galaxies with similar values of Z_{star} and Z_{gas} although the metal yields presented in Fig. 4 can differ by orders of magnitude. This stems from the fact that the metal injection is dominated by SNe. Anyway, Z_{star} and Z_{gas} are nearly 30 per cent lower in the E9B and E10B simulations compared to the corresponding O and R runs.

On the one hand, the metallicities of our galaxies at $z = 3$ are in very good agreement with those found in other simulations for objects with similar stellar masses and using an early-feedback scheme (e.g. Ma et al. 2016). On the other hand, they appear to be low compared to estimates based on observational data (e.g. Sommariva et al. 2012; Arabsalmami et al. 2018) which, however, are known to suffer from uncertain calibrations.

False-colour images of the simulated galaxies at $z = 3$ are displayed in Figs. 6 and 7 for the low- and high-resolution sets, respectively. In all cases, the reference system has been rotated based on the angular momentum of the stars to present the face-on and edge-on projections. The images in the top rows (orange tones) show the maximum gas density along each line of sight while those in the bottom rows (blue tones) show the projected positions of the individual stellar particles (colour coded according to their local density determined with a spherical cubic-spline kernel). Generally, the galaxies assume the shape of oblate ellipsoids. The gas distribution is more extended than the stellar one and shows many filamentary features in the outskirts resulting either from interactions with satellite systems or large-scale flows. Most of the SN-only models (S9T, S10T and E9S) present dense gaseous and stellar concentrations at their centres, while those accounting for stellar winds are more uniform and flattened (disc like).

5.2 Stellar mass versus halo mass

The stellar mass - halo mass relation (SMHMR) provides a convenient way to test whether our simulations are compatible with observations or not. This semi-empirical relation is obtained by matching DM haloes from N -body simulations to estimates for the stellar mass of galaxies in a catalogue under the assumption that M_{\star} scales monotonically with the halo mass. In Fig. 8, we show SMHMRs obtained at $z = 3$ by different authors (smooth solid lines, Behroozi et al. 2013, hereafter B13; Moster et al. 2013, hereafter M13; Behroozi et al. 2019, hereafter B19) together with their uncertainty (shaded regions). These estimates consistently show that the conversion of baryons into stars is most efficient within haloes with a mass of $\sim 10^{12} M_{\odot}$ where M_{\star}/M_{vir} is of the order of a per cent. In order to

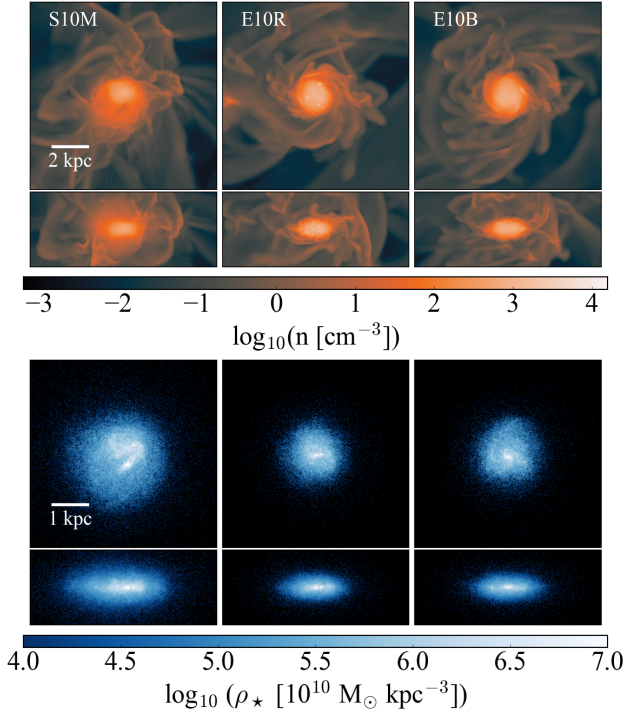


Figure 7. As in Fig. 6 but for the high-resolution simulations.

compare these results with our simulations we extrapolate the fits in the literature to lower halo masses (dashed lines) for which data are not available. The wiggly lines in the left-hand side of Fig. 8 show the trajectories of our simulated galaxies in the $M_{\text{vir}}-M_*$ plane within the redshift range $9 > z \geq 3$. Time runs from left to right and the coloured circles highlight the end point at $z = 3$. All models (with the exception of S9T) are very close in the $M_{\text{vir}}-M_*$ plane at $z = 9$ but they separate more and more with time. A rather sharp decrease in the stellar-to-halo mass ratio is caused at $z \approx 5.2$ by a major-merger event which increases the halo mass. By comparing the position of the symbols to the fits from the literature, we conclude that the SN-only models are unable to efficiently regulate their SF via feedback and produce too many stars. On the other hand, including winds brings the simulations in rather good agreement with the SMHMR (within the statistical uncertainties). This holds true for both the low- and high-resolution runs and suggests that our numerical set up provides converged global properties for the simulated galaxies. At earlier times (and thus for lower halo masses), the simulated galaxies are systematically shifted towards higher stellar masses with respect to the extrapolated SMHMR at $z = 3$. However, this is fully consistent with estimates of the SMHMR at higher redshifts (see, e.g. fig. 9 in B19).

5.3 Stellar profiles

Early stellar feedback plays a key role in shaping galaxies as it maintains gas hot and creates pressure support which prevents low-angular-momentum material from reaching the central regions (Stinson et al. 2013). The net effect is that smaller bulges are assembled. The (face-on) projected stellar surface-density profiles of the three galaxies simulated at high resolution (Fig. 9) show that S10M is denser than E10R and E10B at all radii, while the runs including winds present nearly identical profiles. Towards the galactic centre,

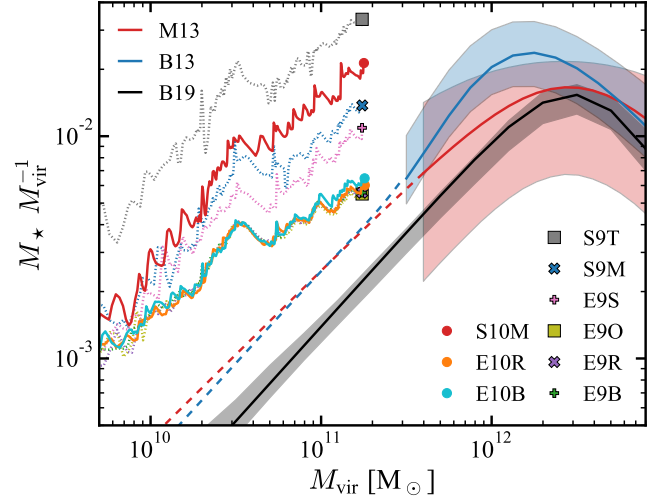


Figure 8. The trajectories of the simulated galaxies in the $M_{\text{vir}}-M_*$ plane during the redshift interval $9 > z \geq 3$ (wiggly lines with the end point indicated by a solid symbol) are compared with the SMHMR at $z = 3$ as determined by B13, M13 and B19. Note that all trajectories extracted from simulations that account for stellar winds overlap almost perfectly.

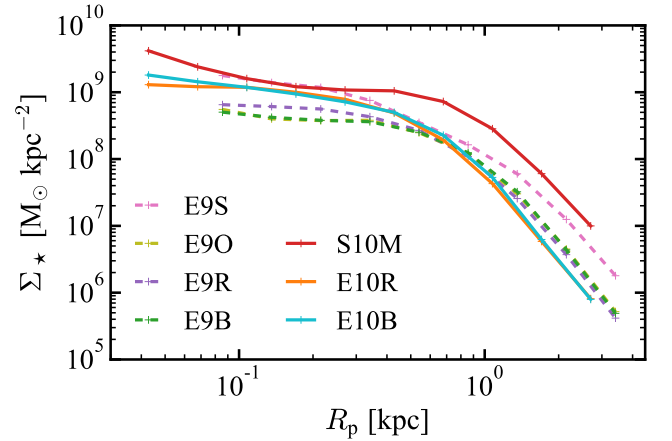


Figure 9. Face-on stellar surface-density profiles for the high-resolution and selected low-resolution runs at $z = 3$.

S10M shows a conspicuous increase in the stellar density while the E-simulations exhibit a nearly constant-density core. This difference is even more marked in the outskirts of the galaxy where S10M is ~ 10 times denser. It is worth mentioning that the profiles rapidly decline beyond 1 kpc thus indicating that the stellar distributions are much more compact than R_{gal} . In order to distinguish between the impact of the time-dependent SN feedback and of the wind feedback, in Fig. 9, we also display the results for the E9 simulations. Note that the run with the time-dependent SN feedback and no winds (E9S) produces a denser stellar profile (similar to S10M) compared to the galaxies simulated accounting for stellar winds (E9O, E9R and E9B).

The energy injection from winds and SN into the ISM is isotropic implying that, in a disc galaxy, feedback plays an important role in moulding the vertical surface-density profiles of the stars. This quantity is analysed in the top panel of Fig. 10 (where we use a rectangular window with transverse size $2R_{\text{gal}}$). Apart from the different

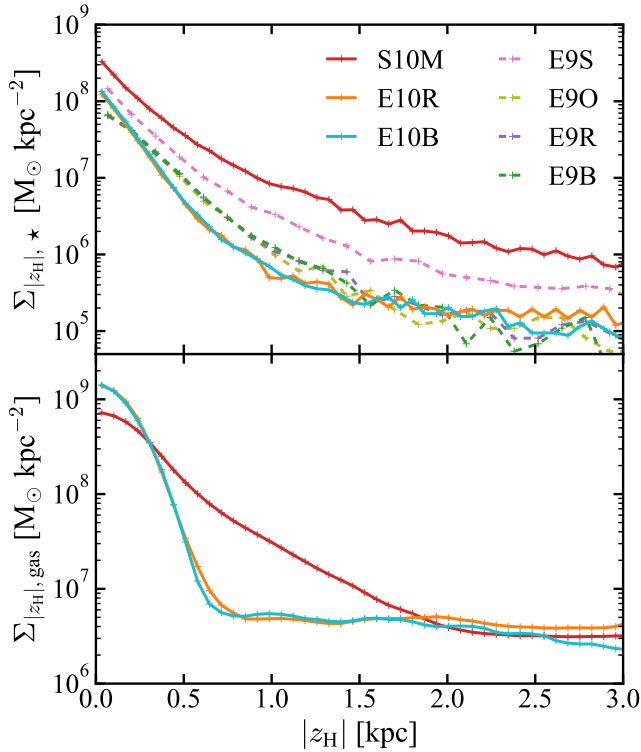


Figure 10. Edge-on surface-density profiles for the stars (top panel) and gas (bottom panel) in the high-resolution and selected low-resolution simulations at $z = 3$.

overall normalization, the stellar distribution in the S10M model is less flattened than in the E-counterparts (see also Fig. 7). The profile extracted from the E9S run lies in between those obtained from the other E9 and the S10M simulations, so the continuous SNe injection only partially accounts for the drop in the stellar density. Keeping this in mind, we will only consider the high-resolution runs in the remainder of this paper.

In order to measure the kinematic state of the stellar orbits, we consider the velocity anisotropy parameter,

$$\beta = 1 - \frac{\sigma_{\text{Tan}}^2}{2\sigma_{\text{Rad}}^2}, \quad (7)$$

where σ_{Tan} and σ_{Rad} denote the tangential and radial velocity dispersions, respectively. If all orbits in a system are purely radial passing through the galactic centre, then $\beta = 1$. If, instead, they are all circular, then $\beta \rightarrow -\infty$. A system with an isotropic velocity distribution has $\beta = 0$. In the top panel of Fig. 11, we show the radial profiles of β for our high-resolution runs. The shapes of the profiles look very similar in the different simulations but β is more biased towards radial orbits in the S10M run, at least within the central 2 kpc. The two E-simulations have almost identical profiles which are nearly isotropic in the centre ($R < 0.2$ kpc) and are radially biased in the outskirts. The stellar kinematic in the E10R and E10B galaxies thus reveals the presence of a more pronounced disc-like structure than in S10M. On the other hand, all models present a tenuous stellar halo which is also discernible in the Σ_* -profiles for $R > 1$ kpc.

The radial mass-weighted age profiles of the stellar populations at $z = 3$ are presented in the bottom panel of Fig. 11. For all galaxies, the mean stellar age increases with R but it turns out that the stars in

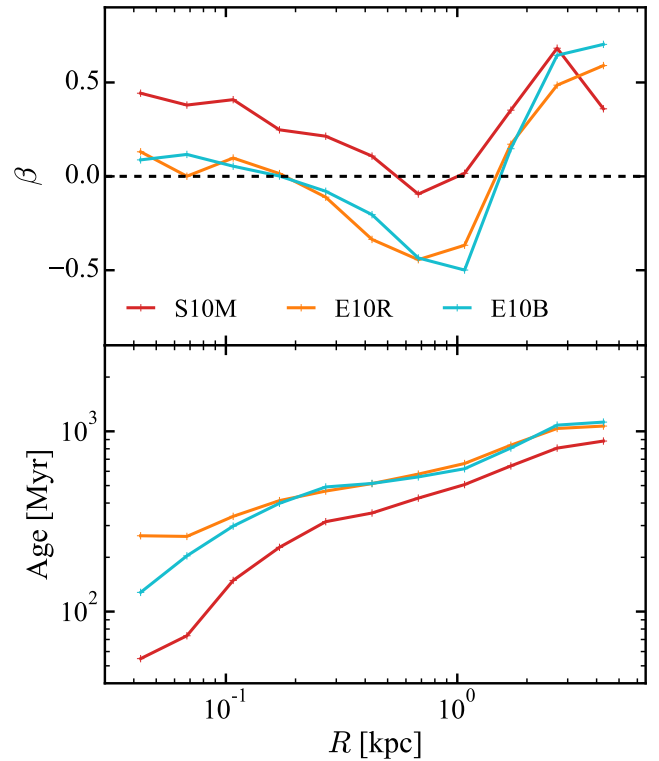


Figure 11. Spherical radial profiles of the velocity anisotropy parameter (top panel) and of the mass-weighted stellar age (bottom panel) at $z = 3$.

S10M are on average younger than in E10R and E10B at all radii. The difference is more pronounced in the central regions ($R < 0.2$ kpc) which have been actively forming stars shortly before $z = 3$ (see also Fig. 12). This reflects the higher efficiency of early stellar feedback in regulating local star formation.

5.4 Gas profiles

It is interesting to investigate how the gas and stellar distributions in the simulated galaxies relate to each other. In the bottom panel of Fig. 10, we show the edge-on surface-density profiles of the gas at $z = 3$. The gas distribution in the E10R and E10B galaxies is more concentrated than in S10M and reaches higher densities at the centre (which compensates for the lower stellar content). The gas profiles of the E-models, however, show an abrupt decline at $|z_H| \approx 0.6$ kpc which can be used to define the edge of the galaxies. Additionally, this decline marks a clear transition between a disc-like structure and its surrounding halo, which is not present in the S10M galaxy. We conclude that the E10R and E10B galaxies present a flatter, more disc-like gas distribution than S10M (see also the top panels in Fig. 7).

The top panel of Fig. 12 presents the spherical gas-density profiles (solid lines) for the galaxies at $z = 3$ while the middle panel shows the mass fractions of ‘cold’ ($T < 2 \times 10^4$ K, from which stars form in the simulations) and hot ($T > 2 \times 10^4$ K) gas as a function of the distance from the galaxy centre. Remarkably, the E-simulations contain ten times more gas at their centres than the S10M model. In all cases, the gas density stays nearly constant for $R \lesssim 0.6$ kpc and drops rapidly at larger distances. All the gas in this extended region with uniform density is hot due to the presence of young stars which

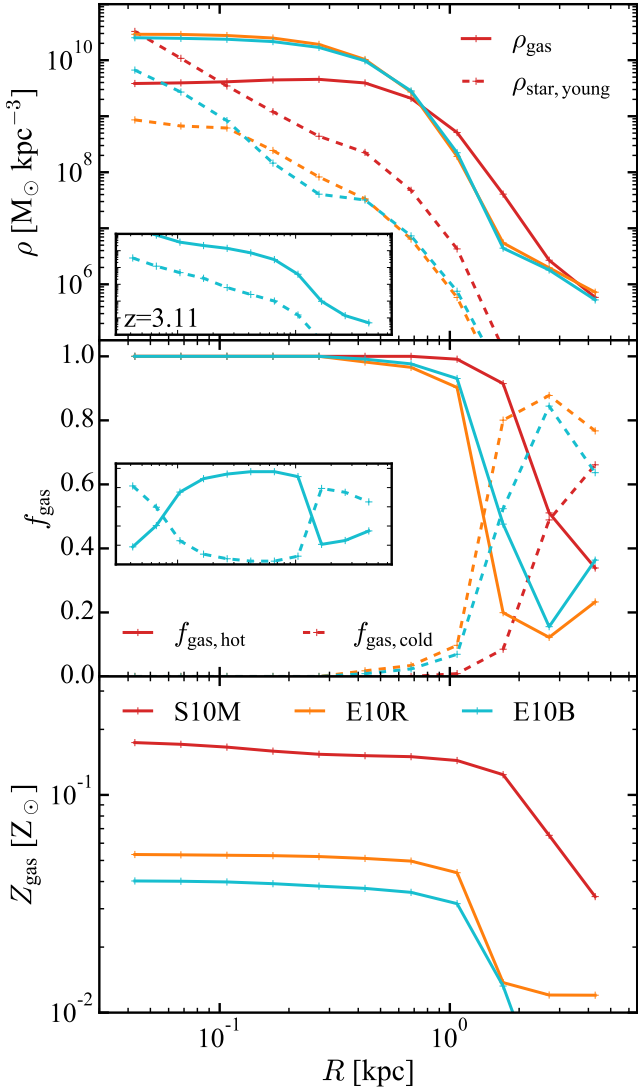


Figure 12. Spherical radial profiles for different galaxy properties at $z = 3$. The top panel shows the mass-density profiles for the gas (solid) and for the recently formed stars ($t_* < 50$ Myr, dashed). The middle panel reveals the radial dependence of the fractions of cold and hot gas. Finally, the bottom panel displays the average metallicity of the gas. The insets in the top two panels refer to the E10B galaxy at $z = 3.11$ and have compressed axes that represent the same range as the extended panels.

have recently injected energy into the ISM. Cold gas is only present in the outer regions where little or no star formation took place in the recent past. The galaxies at $z = 3$ happen to be in a transient sterilised state: feedback from a recent star-formation episode prevents new star formation (see also Section 5.5). In order to demonstrate that this is indeed the case, in the insets of the top and middle panels we show again the profiles for the E10B galaxy but this time we evaluate them at $z = 3.11$ (i.e. approximately 80 Myr before $z = 3$): the presence of cold and dense gas in the central regions now makes star formation possible.

The bottom panel of Fig. 12 shows the metallicity profiles of the ISM. As already seen in Table 2, the S10M galaxy is substantially more metal rich than the E-runs (by a factor 2.9 and 4 with respect to E10R and E10B, respectively) but the shape of the metal distribution

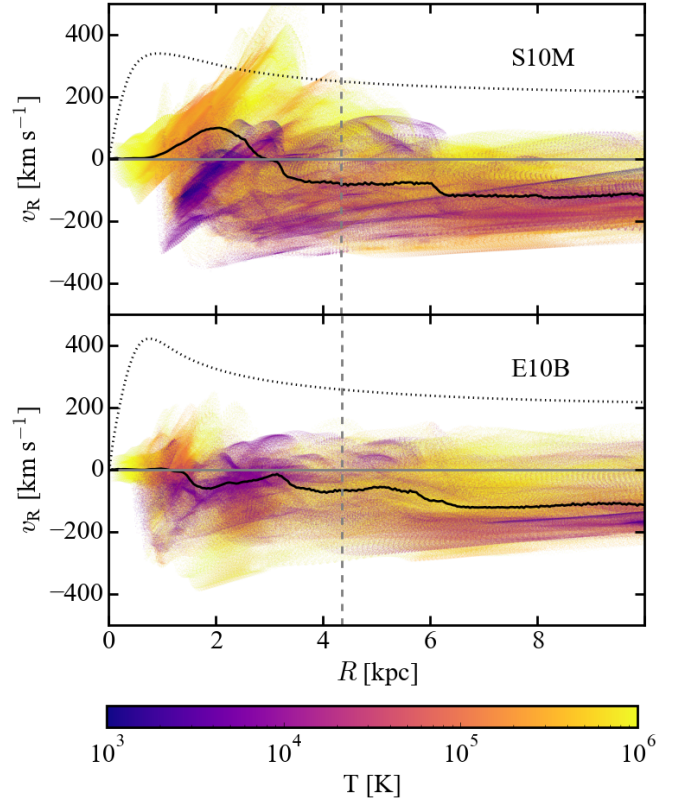


Figure 13. Radial phase-space diagrams for the gas in the S10M (top panel) and E10B (bottom panel) simulations at $z = 3$. The colour coding reflects the gas temperature while the solid and dotted black lines represent the mass-weighted mean radial velocity and the escape velocity, respectively. The vertical dashed grey line indicates the galaxy radius R_{gal} .

is similar in all objects with an extended uniform core and a rapidly declining profile for $R \gtrsim 1.5$ kpc. This drop reflects the finite size of the stellar components, the feedback efficiency in expelling metals, and the infall of metal-poor gas from the circumgalactic medium. The lower metal content of the E-galaxies makes gas cooling less efficient and thus halts the formation of new stars for longer times after a burst of star formation takes place. The different normalization of the metal profiles in E10R and E10B is a direct consequence of the yields shown in Fig. 4.

5.5 Outflows and metal enrichment

In Fig. 13, we present radial phase-space diagrams of the gas component at $z = 3$ colour-coded by temperature. Outflows of hot gas with radial velocities exceeding the escape velocity (dotted line) are clearly noticeable in the S10M galaxy (top panel). The (mass-weighted) mean gas velocity (solid line) is positive for $R < 3.0$ kpc (with a peak value of 100 km s^{-1}) and negative at larger radii implying that there is a net inflow of material within R_{gal} (vertical dashed line). The E10B galaxy (bottom panel) shows a similar net inflow of material but does not present fast outflowing gas that could escape the system.

In order to better understand how early and SN feedback influence galactic outflows and push the gas into the circumgalactic medium, in Fig. 14, we compare the inward and outward mass-flow rates calculated at $R = 2$ kpc with the SFR of the simulated galaxies (averaged over a time-span of 10 Myr). The first thing to notice is

that star formation is bursty in both galaxies (as expected from a self-regulating process) but the amplitude of the variations is much larger in S10M – the coefficient of variation CV (i.e. the ratio of the standard deviation of the SFR to the mean) is twice as large than in E10B (namely, $CV_{S10M} = 2.6$ while $CV_{E10B} = 1.3$). The highest peaks of star formation trigger gas outflows that go past 2 kpc (like the one at $z \approx 4.8$ following a major galaxy merger). These outflow maxima are followed by sudden increases of the inflow rates, suggesting that a galactic fountain is in place. These features are much more prominent in S10M than in E10B.

All this is consistent with the picture in which stellar winds heat up the ISM and locally inhibit further star formation thus leading to a more uniform star-formation history. The reduced (and less spatially clustered) SN activity is then unable to launch high-speed galactic winds. This is in line with the recent finding that early stellar feedback suppresses galactic outflows in galaxies hosted by lower-mass haloes than those considered here (Smith et al. 2021).

It is worth noticing that also the mass-inflow rates at $R = 2$ kpc are lower in E10B than in S10M. This could be for two reasons: (i) since outflows are weaker, there is less material that could fall back and/or (ii) the infall of recycled and pristine gas on to the galaxies is prevented by early feedback which keeps the gas hot.

Finally, we investigate if metals ejected by stellar winds follow a different spatial distribution than those ejected by SNe. In a recent theoretical study aiming at explaining the large observed scatter of N/O at low O/H, Roy et al. (2021) conjectured that wind metals are more likely to remain locked up within a low-metallicity dwarf galaxy than SN metals. We test whether this scenario takes place in our simulated galaxies which, however, are hosted by substantially more massive haloes than those analysed in Roy et al. (2021). The spherical radial profiles for the E10B galaxy at $z = 3$ shown in Fig. 15 reveal that nearly 90 per cent of the metals which are found within R_{gal} (and 80 per cent of those at R_{vir}) have been ejected by SNe. The mean metallicities generated by winds and SNe stay basically constant in the innermost regions (where also the stars are found) and suddenly drop by an order of magnitude at $R \approx 1.5$ kpc revealing that the circumgalactic medium is relatively metal poor (the sharp peak around $R = 10$ kpc is due to a satellite galaxy). Maps of the relative distribution of metals due to winds and SNe (Fig. 16) confirm that the two types of metals are very well mixed within the galaxy. This reflects the fact that the material emitted by winds does not travel very far from the massive stars and is subsequently swept up by the faster SN ejecta. Beyond the galaxy, the maps are more complex due to the interplay of gas accretion, outflows, and the presence of satellite galaxies (passing by or being ripped apart). Apart from a few localized features, a general trend is noticeable: the relative importance of wind metals slightly increases with R , probably due to the Z dependence of the wind-metal ejecta (see Fig. 4).

6 SUMMARY

Main-sequence and post-main-sequence winds from massive stars provide a continuous injection of kinetic energy, mass, and metals into the ISM. In order to quantify the corresponding yields, we compute different sets of evolutionary tracks using the MESA code and accounting for the presence of binary systems and of a metallicity-dependent distribution of initial rotational velocities. We find that:

(i) For the most-massive models, the ratio between the kinetic-energy yields of stellar winds and SNe ranges from a few per cent to more than a hundred per cent depending on the input parameters

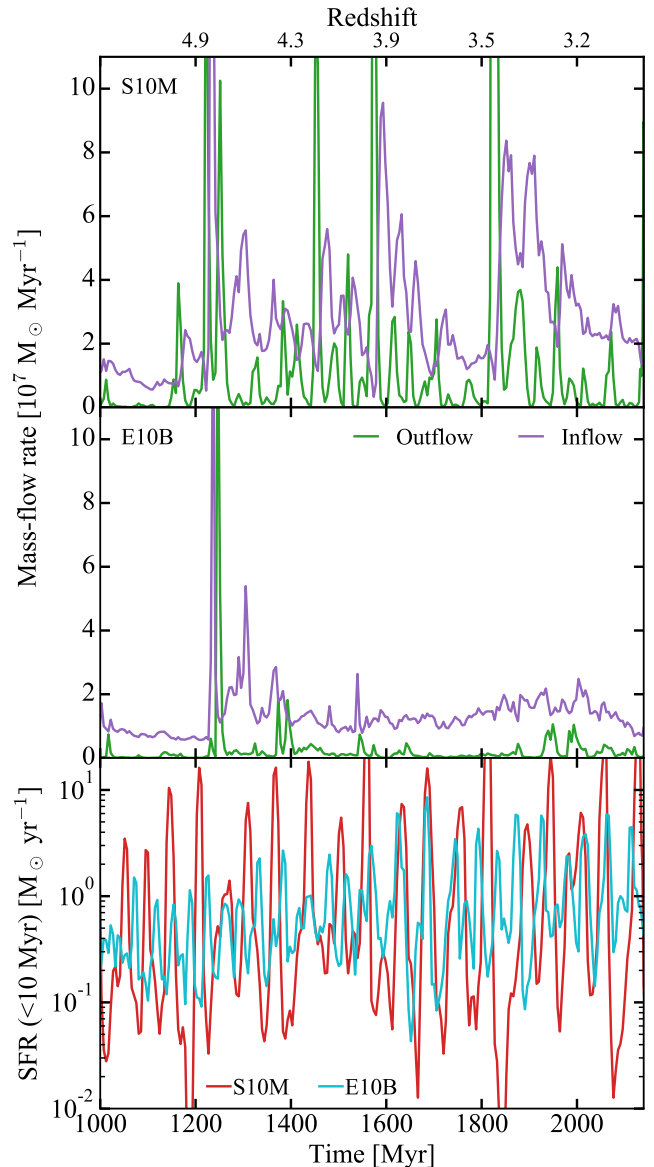


Figure 14. The inward and outward gas-mass flow rates measured at $R = 2$ kpc in the S10M (top panel) and E10B (middle panel) galaxies are compared with the corresponding SFR averaged over 10 Myr (bottom panel).

(Z , v_{ini} , binarity). Crucially, this energy becomes available on time-scales shorter than the free-fall time of a young cluster.

(ii) A stellar population consisting of rotating and binary stars generates substantially stronger mechanical feedback compared to standard models based on single non-rotating stars, especially at low metallicity. In fact, both binaries and rotation significantly flatten the otherwise steep metallicity dependence of the mechanical-energy yield (see Section 2.3). Additionally, the mass and metal yields are also enhanced.

As a second step, we implement the feedback yields derived from our stellar evolutionary models into RAMSES and run a suite of simulations which follow the formation and evolution of a galaxy until redshift 3 (at which we achieve a nominal spatial resolution of 34 pc). We follow the central galaxy hosted by a DM halo with a final mass of $1.8 \times 10^{11} M_{\odot}$ and use the same IC to compare the galaxies generated

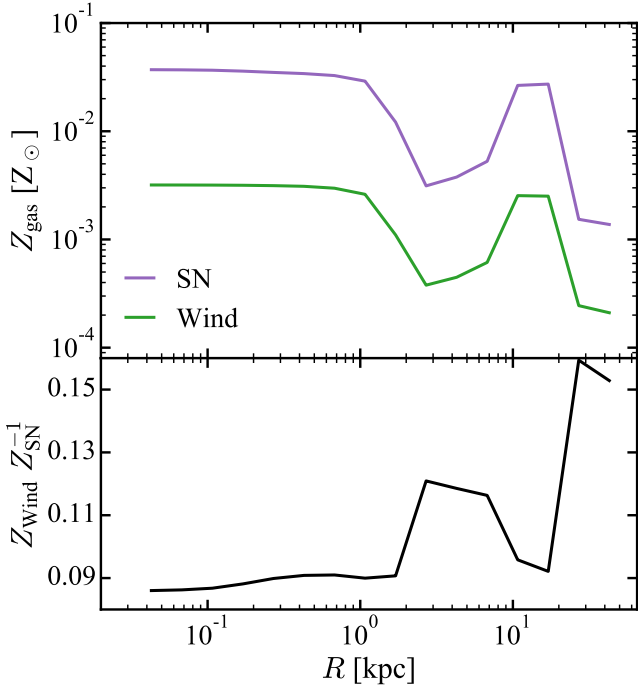


Figure 15. Top panel: spherical radial profiles of the mass-weighted gas metallicity (for the E10B galaxy at $z = 3$) obtained by separating the contributions from the metals entrained in stellar winds and from those ejected by SNe. Bottom panel: ratio between the profiles shown in the top panel.

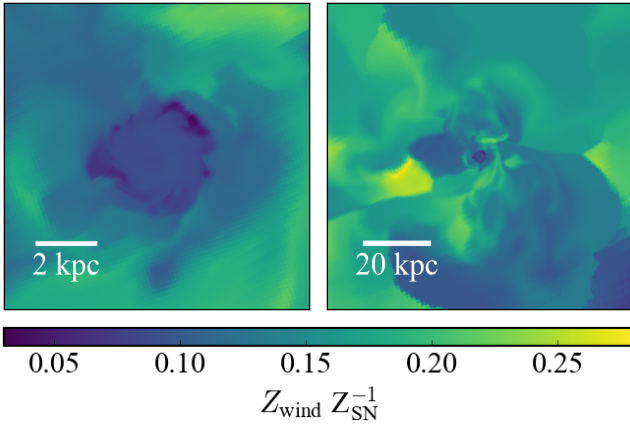


Figure 16. Face-on maps of the ratio between the wind- and SN-generated metallicities for the E10B galaxy (left-hand panel) and its halo (right-hand panel) at $z = 3$.

with different versions of our early feedback scheme (E models) with the galaxy obtained considering SN-only feedback in the standard RAMSES implementation (S model). For the E models, we consider three different options: non-rotating single stars, rotating single stars, and a mix of rotating single stars and binary stars.

It is important to stress that modelling stellar mass-loss requires a number of assumptions and even our detailed evolutionary models bear large uncertainties. The complex interaction of the wind ejecta with the circumstellar material introduces further uncertainties in the calculations (see the discussion in Section 2.4). In the absence

of a consensus in the literature regarding the fraction of emitted energy which is dissipated into heat on sub-grid scales, we inject the whole energy released by the winds and SNe into the ISM and solve the equations of fluid dynamics to determine the gas flows on spatially resolved scales. In this sense, our investigation quantifies the maximum effect that could be possibly driven by stellar winds on galaxy formation. Our main findings are as follows:

- (iii) In the E models, the stellar mass is reduced by a factor of three compared with the S model. This makes sure that the stellar-mass-to-halo-mass ratio is consistent with current semi-empirical estimates (see Fig. 8).
- (iv) The stellar surface-density profile of the E galaxies flattens in the central region, contrary to the outcome of the S model which shows a central cusp (see Fig. 9). Additionally, the stars in the E galaxies have a lower anisotropy parameter, indicating that the structures are more rotationally supported (see Fig. 11).
- (v) Accounting for wind feedback leads to a smoother and less bursty SFR, less strong outflows and even reduced accretion flows.
- (vi) All the E galaxies have very similar stellar and gas masses. However, those including binary stars turn out to be more metal poor than those with single stars (while no important difference is noticeable between rotating and non-rotating models). A caveat to this is that we neglect the impact of binarity and rotation on the nucleosynthesis of SNe.
- (vii) The final spatial distribution of the metals which have been entrained in stellar winds or ejected by SNe is very similar within the galaxy and also in the circumgalactic medium. SN metals account for nearly 90 per cent of the total with a slight decrease in the outermost regions.

ACKNOWLEDGEMENTS

We would like to thank R. Teyssier for making the RAMSES code publicly available. We also thank J. Mackey and S. Geen for valuable discussions. Some of the figures were produced using the yt package (Turk et al. 2011). This research has made use of the VizieR catalogue access tool, CDS, Strasbourg, France (Ochsenbein et al. 2000). The original description of the VizieR service was published in 2000, A&AS 143, 23. This work was carried out within the Collaborative Research Centre 956, sub-project C04, funded by the Deutsche Forschungsgemeinschaft (DFG) – project ID 184018867. We gratefully acknowledge the Gauss Centre for Supercomputing e.V. (www.gauss-centre.eu) for funding this project by providing computing time on the GCS Supercomputer SuperMUC-NG at Leibniz Supercomputing Centre (www.lrz.de). We acknowledge the Max-Planck-Society for providing computing time on the MPG Supercomputer Cobra at the Max Planck Computing and Data Facility. YAF is part of the International Max Planck research school in Astronomy and Astrophysics and guest at the Max-Planck-Institute for Radio Astronomy.

DATA AVAILABILITY

The data underlying this article will be shared on reasonable request to the corresponding author.

REFERENCES

Abbott D. C., 1978, *ApJ*, 225, 893

- Agertz O., Kravtsov A. V., 2015, *ApJ*, **804**, 18
- Agertz O., Teyssier R., Moore B., 2011, *MNRAS*, **410**, 1391
- Agertz O., Kravtsov A. V., Leitner S. N., Gnedin N. Y., 2013, *ApJ*, **770**, 25
- Agertz O., et al., 2020, *MNRAS*, **491**, 1656
- Ali A., Harries T. J., Douglas T. A., 2018, *MNRAS*, **477**, 5422
- Almeida L. A., et al., 2017, *A&A*, **598**, A84
- Arabsalmani M., et al., 2018, *MNRAS*, **473**, 3312
- Barnes A. T., Longmore S. N., Dale J. E., Krumholz M. R., Kruijssen J. M. D., Bigiel F., 2020, *MNRAS*, **498**, 4906
- Behroozi P. S., Wechsler R. H., Conroy C., 2013, *ApJ*, **770**, 57
- Behroozi P., Wechsler R., Hearin A., Conroy C., 2019, *MNRAS*, **488**, 3143–3194
- Bending T. J. R., Dobbs C. L., Bate M. R., 2020, *MNRAS*, **495**, 1672
- Benson A. J., 2010, *Phys. Rep.*, **495**, 33
- Böhm-Vitense E., 1958, *Z. Astrophys.*, **46**, 108
- Bouret J. C., Lanz T., Martins F., Marcolino W. L. F., Hillier D. J., Depagne E., Hubeny I., 2013, *A&A*, **555**, A1
- Bragança G. A., Daffon S., Cunha K., Bensby T., Oey M. S., Walth G., 2012, *AJ*, **144**, 130
- Brook C. B., Stinson G., Gibson B. K., Wadsley J., Quinn T., 2012, *MNRAS*, **424**, 1275
- Brott I., et al., 2011, *A&A*, **530**, A115
- Ceverino D., Klypin A., 2009, *ApJ*, **695**, 292
- Chevance M., et al., 2022, *MNRAS*, **509**, 272
- Chiappini C., Hirschi R., Meynet G., Ekström S., Maeder A., Matteucci F., 2006, *A&A*, **449**, L27
- Crain R. A., et al., 2015, *MNRAS*, **450**, 1937
- Creasey P., Theuns T., Bower R. G., 2013, *MNRAS*, **429**, 1922
- Crowther P. A., 2007, *ARA&A*, **45**, 177
- Dale J. E., Bonnell I., 2011, *MNRAS*, **414**, 321
- Dale J. E., Ngoumou J., Ercolano B., Bonnell I. A., 2014, *MNRAS*, **442**, 694
- Davé R., Rafieferantsoa M. H., Thompson R. J., Hopkins P. F., 2017, *MNRAS*, **467**, 115
- De Becker M., Raucq F., 2013, *A&A*, **558**, A28
- de Jager C., Nieuwenhuijzen H., van der Hucht K. A., 1988, *A&AS*, **72**, 259
- De Marco O., Izzard R. G., 2017, *Publ. Astron. Soc. Australia*, **34**, e001
- de Mink S. E., Langer N., Izzard R. G., Sana H., de Koter A., 2013, *ApJ*, **764**, 166
- Dekel A., Silk J., 1986, *ApJ*, **303**, 39
- Doran E. I., et al., 2013, *A&A*, **558**, A134
- Dubois Y., Teyssier R., 2008, *A&A*, **477**, 79
- Dufton P. L., et al., 2006, *A&A*, **457**, 265
- Dufton P. L., et al., 2013, *A&A*, **550**, A109
- Dufton P. L., Evans C. J., Hunter I., Lennon D. J., Schneider F. R. N., 2019, *A&A*, **626**, A50
- Dwarkadas V. V., 2005, *ApJ*, **630**, 892
- Dwarkadas V. V., 2007, *ApJ*, **667**, 226
- Ekström S., et al., 2012, *A&A*, **537**, A146
- Eldridge J. J., Stanway E. R., Xiao L., McClelland L. A. S., Taylor G., Ng M., Greis S. M. L., Bray J. C., 2017, *Publ. Astron. Soc. Australia*, **34**, e058
- Emerick A., Bryan G. L., Mac Low M.-M., 2019, *MNRAS*, **482**, 1304
- Emerick A., Bryan G. L., Mac Low M.-M., 2020, arXiv e-prints, p. arXiv:2007.03702
- Fierlinger K. M., Burkert A., Ntormousi E., Fierlinger P., Schartmann M., Ballone A., Krause M. G. H., Diehl R., 2016, *MNRAS*, **456**, 710
- Gaige Y., 1993, *A&A*, **269**, 267
- García-Segura G., Mac Low M. M., Langer N., 1996a, *A&A*, **305**, 229
- García-Segura G., Langer N., Mac Low M. M., 1996b, *A&A*, **316**, 133
- Gatto A., et al., 2015, *MNRAS*, **449**, 1057
- Gatto A., et al., 2017, *MNRAS*, **466**, 1903
- Geen S., Rosdahl J., Blaizot J., Devriendt J., Slyz A., 2015, *MNRAS*, **448**, 3248
- Geen S., Hennebelle P., Tremblin P., Rosdahl J., 2016, *MNRAS*, **463**, 3129
- Geen S., Bieri R., Rosdahl J., de Koter A., 2021, *MNRAS*, **501**, 1352
- Gerritsen J. P. E., 1997, PhD thesis, -
- Gerritsen J. P. E., Icke V., 1997, *A&A*, **325**, 972
- Gill S. P. D., Knebe A., Gibson B. K., 2004, *MNRAS*, **351**, 399
- Girichidis P., et al., 2016, *MNRAS*, **456**, 3432
- Glebbeeck E., Gaburov E., Portegies Zwart S., Pols O. R., 2013, *MNRAS*, **434**, 3497
- Gnedin N. Y., 1998, *MNRAS*, **294**, 407
- Götberg Y., de Mink S. E., Groh J. H., 2017, *A&A*, **608**, A11
- Götberg Y., de Mink S. E., Groh J. H., Leitherer C., Norman C., 2019, *A&A*, **629**, A134
- Governato F., Willman B., Mayer L., Brooks A., Stinson G., Valenzuela O., Wadsley J., Quinn T., 2007, *MNRAS*, **374**, 1479
- Gräfener G., Vink J. S., 2013, *A&A*, **560**, A6
- Grassitelli L., Langer N., Mackey J., Gräfener G., Grin N. J., Sander A. A. C., Vink J. S., 2021, *A&A*, **647**, A99
- Grazian A., et al., 2015, *A&A*, **575**, A96
- Gutcke T. A., Pakmor R., Naab T., Springel V., 2021, *MNRAS*, **501**, 5597
- Hahn O., Abel T., 2011, *MNRAS*, **415**, 2101
- Haid S., Walch S., Seifried D., Wunsch R., Dinnbier F., Naab T., 2018, *MNRAS*, **478**, 4799
- Haid S., Walch S., Seifried D., Wunsch R., Dinnbier F., Naab T., 2019, *MNRAS*, **482**, 4062
- Heney L., Vardya M. S., Bodenheimer P., 1965, *ApJ*, **142**, 841
- Hirai Y., Fujii M. S., Saitoh T. R., 2021, *PASJ*, **73**, 1036
- Hopkins P. F., Quataert E., Murray N., 2011, *MNRAS*, **417**, 950
- Hopkins P. F., Kereš D., Oñorbe J., Faucher-Giguère C.-A., Quataert E., Murray N., Bullock J. S., 2014, *MNRAS*, **445**, 581
- Hopkins P. F., et al., 2018, *MNRAS*, **480**, 800
- Howard C. S., Pudritz R. E., Harris W. E., 2016, *MNRAS*, **461**, 2953
- Hu C.-Y., Naab T., Walch S., Glover S. C. O., Clark P. C., 2016, *MNRAS*, **458**, 3528
- Hu C.-Y., Naab T., Glover S. C. O., Walch S., Clark P. C., 2017, *MNRAS*, **471**, 2151
- Huang W., Gies D. R., 2006, *ApJ*, **648**, 580
- Huang W., Gies D. R., McSwain M. V., 2010, *ApJ*, **722**, 605
- Hultman J., Pharasyn A., 1999, *A&A*, **347**, 769
- Humphreys R. M., Davidson K., 1994, *PASP*, **106**, 1025
- Hunter I., Lennon D. J., Dufton P. L., Trundle C., Simón-Díaz S., Smartt S. J., Ryans R. S. I., Evans C. J., 2008, *A&A*, **479**, 541
- Iffrig O., Hennebelle P., 2015, *A&A*, **576**, A95
- Ivanova N., et al., 2013, *A&ARv*, **21**, 59
- Kannan R., Vogelsberger M., Marinacci F., McKinnon R., Pakmor R., Springel V., 2019, *MNRAS*, **485**, 117
- Katz N., 1992, *ApJ*, **391**, 502
- Keller S. C., 2004, *Publ. Astron. Soc. Australia*, **21**, 310
- Kereš D., Katz N., Weinberg D. H., Davé R., 2005, *MNRAS*, **363**, 2
- Kim C.-G., Ostriker E. C., 2015, *ApJ*, **802**, 99
- Kim C.-G., Ostriker E. C., 2017, *ApJ*, **846**, 133
- Kim J.-G., Kim W.-T., Ostriker E. C., 2016, *ApJ*, **819**, 137
- Kim J.-G., Kim W.-T., Ostriker E. C., 2018, *ApJ*, **859**, 68
- Kimm T., Cen R., 2014, *ApJ*, **788**, 121
- Knollmann S. R., Knebe A., 2009, *ApJS*, **182**, 608
- Kobulnicky H. A., et al., 2014, *ApJS*, **213**, 34
- Körtgen B., Seifried D., Banerjee R., Vázquez-Semadeni E., Zamora-Avilés M., 2016, *MNRAS*, **459**, 3460
- Kretschmer M., Teyssier R., 2020, *MNRAS*, **492**, 1385
- Kroupa P., 2001, *MNRAS*, **322**, 231
- Lahén N., Naab T., Johansson P. H., Elmegreen B., Hu C.-Y., Walch S., 2019, *ApJ*, **879**, L18
- Lahén N., Naab T., Johansson P. H., Elmegreen B., Hu C.-Y., Walch S., Steinwandel U. P., Moster B. P., 2020, *ApJ*, **891**, 2
- Lancaster L., Ostriker E. C., Kim J.-G., Kim C.-G., 2021, *ApJ*, **914**, 90
- Langer N., Yoon S. C., Petrovic J., Heger A., 2004, *Symposium - International Astronomical Union*, **215**, 535
- Langer N., et al., 2020, *A&A*, **638**, A39
- Leitherer C., Robert C., Drissen L., 1992, *ApJ*, **401**, 596
- Leitherer C., et al., 1999, *The Astrophysical Journal Supplement Series*, **123**, 3–40
- Leitherer C., Ortiz Otálvaro P. A., Bresolin F., Kudritzki R.-P., Lo Faro B., Pauldrach A. W. A., Pettini M., Rix S. A., 2010, *ApJS*, **189**, 309
- Leitherer C., Ekström S., Meynet G., Schaerer D., Agienko K. B., Levesque E. M., 2014, *ApJS*, **212**, 14

- Li M., Tonnesen S., 2020, *ApJ*, **898**, 148
- Li M., Bryan G. L., Ostriker J. P., 2017, *ApJ*, **841**, 101
- Li M., Li Y., Bryan G. L., Ostriker E. C., Quataert E., 2020, *ApJ*, **898**, 23
- Lucas W. E., Bonnell I. A., Dale J. E., 2020, *MNRAS*, **493**, 4700
- Ma X., Hopkins P. F., Faucher-Giguère C.-A., Zolman N., Muratov A. L., Kereš D., Quataert E., 2016, *MNRAS*, **456**, 2140
- Mandel I., de Mink S. E., 2016, *MNRAS*, **458**, 2634
- Marchant P., Langer N., Podsiadlowski P., Tauris T. M., Moriya T. J., 2016, *A&A*, **588**, A50
- Marinacci F., Sales L. V., Vogelsberger M., Torrey P., Springel V., 2019, *MNRAS*, **489**, 4233
- Martayan C., Frémat Y., Hubert A. M., Floquet M., Zorec J., Neiner C., 2006, *A&A*, **452**, 273
- Martayan C., Frémat Y., Hubert A. M., Floquet M., Zorec J., Neiner C., 2007, *A&A*, **462**, 683
- Martayan C., Floquet M., Hubert A. M., Neiner C., Frémat Y., Baade D., Fabregat J., 2008, *A&A*, **489**, 459
- Martizzi D., Faucher-Giguère C.-A., Quataert E., 2015, *MNRAS*, **450**, 504
- McKee C. F., Ostriker J. P., 1977, *ApJ*, **218**, 148
- Mihos J. C., Hernquist L., 1994, *ApJ*, **437**, 611
- Moffat A. F. J., Drissen L., Lamontagne R., Robert C., 1988, *ApJ*, **334**, 1038
- Mokiem M. R., et al., 2006, *A&A*, **456**, 1131
- Mokiem M. R., et al., 2007, *A&A*, **465**, 1003
- Mori M., Yoshii Y., Tsujimoto T., Nomoto K., 1997, *ApJ*, **478**, L21
- Moster B. P., Naab T., White S. D. M., 2013, *MNRAS*, **428**, 3121
- Murante G., Monaco P., Giovalli M., Borgani S., Diaferio A., 2010, *MNRAS*, **405**, 1491
- Navarro J. F., White S. D. M., 1993, *MNRAS*, **265**, 271
- Ngoumou J., Hubber D., Dale J. E., Burkert A., 2015, *ApJ*, **798**, 32
- Norman C. A., Ikeuchi S., 1989, *ApJ*, **345**, 372
- Nugis T., Lamers H. J. G. L. M., 2000, *A&A*, **360**, 227
- Ochsenbein F., Bauer P., Marcout J., 2000, *A&AS*, **143**, 23
- Ocvirk P., et al., 2020, *MNRAS*, **496**, 4087
- Oppenheimer B. D., Davé R., Kereš D., Fardal M., Katz N., Kollmeier J. A., Weinberg D. H., 2010, *MNRAS*, **406**, 2325
- Paczynski B., 1976, in Eggleton P., Mitton S., Whelan J., eds, *IAU Symposium Vol. 73, Structure and Evolution of Close Binary Systems*. p. 75
- Paxton B., Bildsten L., Dotter A., Herwig F., Lesaffre P., Timmes F., 2011, *ApJS*, **192**, 3
- Paxton B., et al., 2013, *ApJS*, **208**, 4
- Paxton B., et al., 2015, *ApJS*, **220**, 15
- Paxton B., et al., 2018, *ApJS*, **234**, 34
- Paxton B., et al., 2019, *ApJS*, **243**, 10
- Penny L. R., Gies D. R., 2009, *ApJ*, **700**, 844
- Perret V., Renaud F., Epinat B., Amram P., Bournaud F., Contini T., Teyssier R., Lambert J.-C., 2014, *A&A*, **562**, A1
- Pillepich A., et al., 2018, *MNRAS*, **473**, 4077
- Planck Collaboration VI 2020, *A&A*, **641**, A6
- Podsiadlowski P., Joss P. C., Hsu J. J. L., 1992, *ApJ*, **391**, 246
- Puls J., Vink J. S., Najarro F., 2008, *aapr*, **16**, 209
- Ramachandran V., Hamann W. R., Hainich R., Oskinova L. M., Shenar T., Sander A. A. C., Todt H., Gallagher J. S., 2018, *A&A*, **615**, A40
- Ramachandran V., et al., 2019, *A&A*, **625**, A104
- Ramírez-Agudelo O. H., et al., 2013, *A&A*, **560**, A29
- Rathjen T.-E., et al., 2021, *MNRAS*, **504**, 1039
- Rey-Raposo R., Dobbs C., Agertz O., Alig C., 2017, *MNRAS*, **464**, 3536
- Rivinius T., Carciofi A. C., Martayan C., 2013, *A&ARv*, **21**, 69
- Rogers H., Pittard J. M., 2013, *MNRAS*, **431**, 1337
- Rosdahl J., Schaye J., Dubois Y., Kimm T., Teyssier R., 2017, *MNRAS*, **466**, 11
- Rosen A. L., Lopez L. A., Krumholz M. R., Ramirez-Ruiz E., 2014, *MNRAS*, **442**, 2701
- Rosen A. L., Offner S. S. R., Foley M. M., Lopez L. A., 2021, arXiv e-prints, p. [arXiv:2107.12397](https://arxiv.org/abs/2107.12397)
- Roy A., Dopita M. A., Krumholz M. R., Kewley L. J., Sutherland R. S., Heger A., 2021, *MNRAS*, **502**, 4359
- Rozyczka M., Tenorio-Tagle G., Franco J., Bodenheimer P., 1993, *MNRAS*, **261**, 674
- Sana H., et al., 2012, *Science*, **337**, 444
- Sana H., et al., 2013, *A&A*, **550**, A107
- Sanyal D., Grassitelli L., Langer N., Bestenlehner J. M., 2015, *A&A*, **580**, A20
- Scannapieco C., et al., 2012, *MNRAS*, **423**, 1726
- Schaller G., Schaerer D., Meynet G., Maeder A., 1992, *A&AS*, **96**, 269
- Schaye J., Dalla Vecchia C., 2008, *MNRAS*, **383**, 1210
- Schmidt M., 1959, *ApJ*, **129**, 243
- Schneider F. R. N., Podsiadlowski P., Langer N., Castro N., Fossati L., 2016, *MNRAS*, **457**, 2355
- Silich S., Tenorio-Tagle G., 2013, *ApJ*, **765**, 43
- Simón-Díaz S., Herrero A., 2014, *A&A*, **562**, A135
- Simpson C. M., Pakmor R., Marinacci F., Pfrommer C., Springel V., Glover S. C. O., Clark P. C., Smith R. J., 2016, *ApJ*, **827**, L29
- Skinner M. A., Ostriker E. C., 2015, *ApJ*, **809**, 187
- Smith N., 2014, *ARA&A*, **52**, 487
- Smith M. D., Rosen A., 2003, *MNRAS*, **339**, 133
- Smith M. C., Sijacki D., Shen S., 2019, *MNRAS*, **485**, 3317
- Smith M. C., Bryan G. L., Somerville R. S., Hu C.-Y., Teyssier R., Burkhardt B., Hernquist L., 2021, *MNRAS*, **506**, 3882
- Sommariva V., Mannucci F., Cresci G., Maiolino R., Marconi A., Nagao T., Baroni A., Grazian A., 2012, *A&A*, **539**, A136
- Sommer-Larsen J., Götz M., Portinari L., 2003, *ApJ*, **596**, 47
- Springel V., Hernquist L., 2003, *MNRAS*, **339**, 289
- Stanway E. R., Eldridge J. J., Becker G. D., 2016, *MNRAS*, **456**, 485
- Stevens I. R., Blondin J. M., Pollock A. M. T., 1992, *ApJ*, **386**, 265
- Stinson G., Seth A., Katz N., Wadsley J., Governato F., Quinn T., 2006, *MNRAS*, **373**, 1074
- Stinson G. S., et al., 2012, *MNRAS*, **425**, 1270
- Stinson G. S., Brook C., Macciò A. V., Wadsley J., Quinn T. R., Couchman H. M. P., 2013, *MNRAS*, **428**, 129
- Strom S. E., Wolff S. C., Dror D. H. A., 2005, *AJ*, **129**, 809
- Sukhbold T., Ertl T., Woosley S. E., Brown J. M., Janka H.-T., 2016, *ApJ*, **821**, 38
- Sundqvist J. O., Owocki S. P., 2013, *MNRAS*, **428**, 1837
- Tajiri Y., Umemura M., 1998, *ApJ*, **502**, 59
- Tenorio-Tagle G., Bodenheimer P., Franco J., Rozyczka M., 1990, *MNRAS*, **244**, 563
- Tenorio-Tagle G., Rozyczka M., Franco J., Bodenheimer P., 1991, *MNRAS*, **251**, 318
- Teyssier R., 2002, *A&A*, **385**, 337
- Teyssier R., Chapon D., Bournaud F., 2010, *ApJ*, **720**, L149
- Thacker R. J., Couchman H. M. P., 2000, *ApJ*, **545**, 728
- Thornton K., Gaudlitz M., Janka H. T., Steinmetz M., 1998, *ApJ*, **500**, 95
- Toalá J. A., Arthur S. J., 2011, *ApJ*, **737**, 100
- Truelove J. K., Klein R. I., McKee C. F., Holliman John H. I., Howell L. H., Greenough J. A., 1997, *ApJ*, **489**, L179
- Turk M. J., Smith B. D., Oishi J. S., Skory S., Skillman S. W., Abel T., Norman M. L., 2011, *The Astrophysical Journal Supplement Series*, **192**, 9
- Usov V. V., 1991, *MNRAS*, **252**, 49
- Valentini M., Murante G., Borgani S., Monaco P., Bressan A., Beck A. M., 2017, *MNRAS*, **470**, 3167
- Van Bever J., Vanbeveren D., 2000, *A&A*, **358**, 462
- Vázquez G. A., Leitherer C., 2005, *ApJ*, **621**, 695
- Vink J. S., 2021, arXiv e-prints, p. [arXiv:2109.08164](https://arxiv.org/abs/2109.08164)
- Vink J. S., de Koter A., Lamers H. J. G. L. M., 2001, *A&A*, **369**, 574
- Vogelsberger M., Genel S., Sijacki D., Torrey P., Springel V., Hernquist L., 2013, *MNRAS*, **436**, 3031
- Walch S., Naab T., 2015, *MNRAS*, **451**, 2757
- Walch S., et al., 2015, *MNRAS*, **454**, 238
- Wechsler R. H., Bullock J. S., Primack J. R., Kravtsov A. V., Dekel A., 2002, *ApJ*, **568**, 52
- Wetzell A. R., Hopkins P. F., Kim J.-h., Faucher-Giguère C.-A., Kereš D., Quataert E., 2016, *ApJ*, **827**, L23
- Wheeler C., et al., 2019, *MNRAS*, **490**, 4447
- Wolff S. C., Strom S. E., Dror D., Venn K., 2007, *AJ*, **133**, 1092
- Wolff S. C., Strom S. E., Cunha K., Daflon S., Olsen K., Dror D., 2008, *AJ*, **136**, 1049

APPENDIX A: MASS YIELD OF THE STELLAR MODELS

A1 Ejected mass of the different stellar models

Fig. A1 shows the fraction of the initial mass that the single star models eject during the different phases of their lifetime. We can see that, even at this relatively low metallicity, our models above $\approx 30 M_{\odot}$ lose between 50 and 80 per cent of their initial mass through their stellar winds, with the most massive models returning several tens of solar masses of material to the ISM on the order of some 10^6 yr. Overall, the fractional ejected mass increases for higher masses. The relative contribution of the OB dwarf phase to the ejected mass is lower compared to the contribution to the kinetic energy. The mass-loss of the non-rotating models below $25 M_{\odot}$ is completely dominated by the RSG phase, in stark contrast with the wind energy (Fig. 1). Instead, for higher masses, the crucial phase appears to be the BSG/LBV phase, where stellar models eject most of their outer, H-rich layers. In fact, while in the top-right corner of the HRD, near or past the so-called Humphreys-Davidson limit (Humphreys & Davidson 1994), the extreme proximity to the Eddington limit (Sanyal et al. 2015; Grassitelli et al. 2021) and the bi-stability mechanism (Vink et al. 2001), lead to mass-loss rates as high as several $10^{-4} M_{\odot} \text{ yr}^{-1}$. For higher rotation velocities, the fraction of ejected mass increases. However, for the highest rotation velocity of 600 km s^{-1} , our most massive stellar models do not evolve toward lower effective temperatures; hence they do not experience neither a BSG/LBV nor a RSG phase. Instead, most of the mass is lost during the WR phases.

Fig. A2 shows the fractional mass-loss of our binary models. In the closest binary systems, the primary fills its Roche lobe and is stripped of the outer, H-rich stellar layers well before it can become a supergiant. As such, most of the mass-loss by stellar wind leaves the system during a cWR phase following the case A mass-transfer phase. However, compared to the single star models, the primary alone reaches helium exhaustion while retaining more of its initial mass, due to the lack of a RSG phase (and a reduced importance of the BSG/LBV phase) with only the evolutionary models more massive than $60 M_{\odot}$ losing more than half of their initial mass. In the longest period binary models, the primary undergoes mass-transfer only once as it approaches its post-main-sequence phase, reducing the overall duration of the cWR phase and, in turn, the fractional mass-loss. None the less, compared to the single star models, the primaries appear to return less material to the ISM. However, we can see that, due to mass-transfer, the secondary stellar model can eject even more than its initial mass (Fig. A2). This includes material which is lost during the mass-transfer phase, in which accretion to the secondary is limited by the model reaching critical rotation (Langer et al. 2004; Paxton et al. 2015). In such a situation, only a limited fraction of material lost by the primary is stably accreted, while the remaining is considered lost via the stellar wind of the accretor. For the primaries, as the single stars, the fractional mass-loss increases towards higher mass. Instead, the lower mass secondaries have higher fractional mass-losses. Considering that mass-transfer takes place predominantly during the secondary's main-sequence, the importance of the post-main-sequence phase is lower compared to the single stars.

A2 Time evolution of the cumulative ejected mass

The fractional mass-loss of a stellar population consisting of single rotating stars up to helium exhaustion is presented in the upper panel of Fig. A3. Colours indicate the mass ejected in each phase. The contribution from the stellar models with lower M_{ini} to the mass budget is higher than for the energy, leading to 45 per cent of the total mass being ejected after the first 5 Myr. The cWR phase is less important, contributing only around 22 per cent of the total. The total mass-loss is dominated by stellar models during the BSG/LBV and the RSG phase, where the RSG phase adds mass after the first 8 Myr when the first lower-mass stars evolve away from the main-sequence.

In comparison with single stars, a population consisting of only binaries ejects a ≈ 30 per cent higher total mass fraction (see lower panel of Fig. A3), mostly due to the contribution of lower mass stars after the first few million years. The increase in the mass yield is due to non-complete accretion of material during the mass-transfer phase, which takes place while the star appears as a OB dwarf. Therefore, the OB dwarf phase has a high contribution for binaries, while the RSG and BSG/LBV phase is relatively more important for single stars.

APPENDIX B: INITIAL ROTATION VELOCITIES

The distribution of initial rotation velocities in a stellar population, $\mathcal{P}(v_{\text{ini}})$, is expected to be metallicity-dependent. In fact, stars with lower metallicities should present higher values of v_{ini} as the loss of angular momentum is less efficient during their formation phase (e.g. Chiappini et al. 2006). Ramírez-Agudelo et al. (2013) measured $\mathcal{P}(v_{\text{ini}})$ for a large sample of O-type stars in the Tarantula nebula and identified two components: a low-velocity peak and a high-velocity tail so that 20 per cent of the population consists of fast rotators with velocities above 300 km s^{-1} . However, the detailed form of $\mathcal{P}(v_{\text{ini}})$ as a function of Z is largely unconstrained primarily due to the limited data available.

In order to get an estimate of the metallicity dependence of $\mathcal{P}(v_{\text{ini}})$, we collect estimates in the literature³ of the projected rotation velocity of young clusters in Galactic (Strom et al. 2005; Dufton et al. 2006; Huang & Gies 2006; Wolff et al. 2007; Martayan et al. 2008; Penny & Gies 2009; Huang et al. 2010; Bragança et al. 2012; Simón-Díaz & Herrero 2014), LMC (Keller 2004; Martayan et al. 2006; Mokiem et al. 2007; Hunter et al. 2008; Wolff et al. 2008; Penny & Gies 2009; Ramírez-Agudelo et al. 2013; Dufton et al. 2013; Ramachandran et al. 2018) and Small Magellanic Cloud (SMC, Mokiem et al. 2006; Martayan et al. 2007; Hunter et al. 2008; Penny & Gies 2009; Bouret et al. 2013; Ramachandran et al. 2019; Dufton et al. 2019) environments. In Fig. B1, we plot the resulting medians and 75th percentiles (together with their standard uncertainties) as a function of Z . We use a weighted least-squares method to fit these estimates with linear relations between the percentiles and $\log(Z)$. We obtain $[(-37 \pm 20) \log(Z/0.0122) + 108 \pm 6] \text{ km s}^{-1}$ for the median and $[(-36 \pm 35) \log(Z/0.0122) + 190 \pm 10] \text{ km s}^{-1}$ for the 75th percentile. The best-fitting value for the slope turns out to be negative as

³ We exclude any samples that are selected by the rotation velocity and any identified binary stars. Evolved stars rotate on average slower due to the loss of angular momentum via stellar wind and the significantly larger radii, therefore we focus the analysis on young open clusters. We disregard instead studies on Be-stars, as stars in such samples are selected for being near-critical rotators (Martayan et al. 2006, 2007; Rivinius et al. 2013). We take the metallicity of the sample either directly from the quoted literature or, if none is provided, from other estimates.

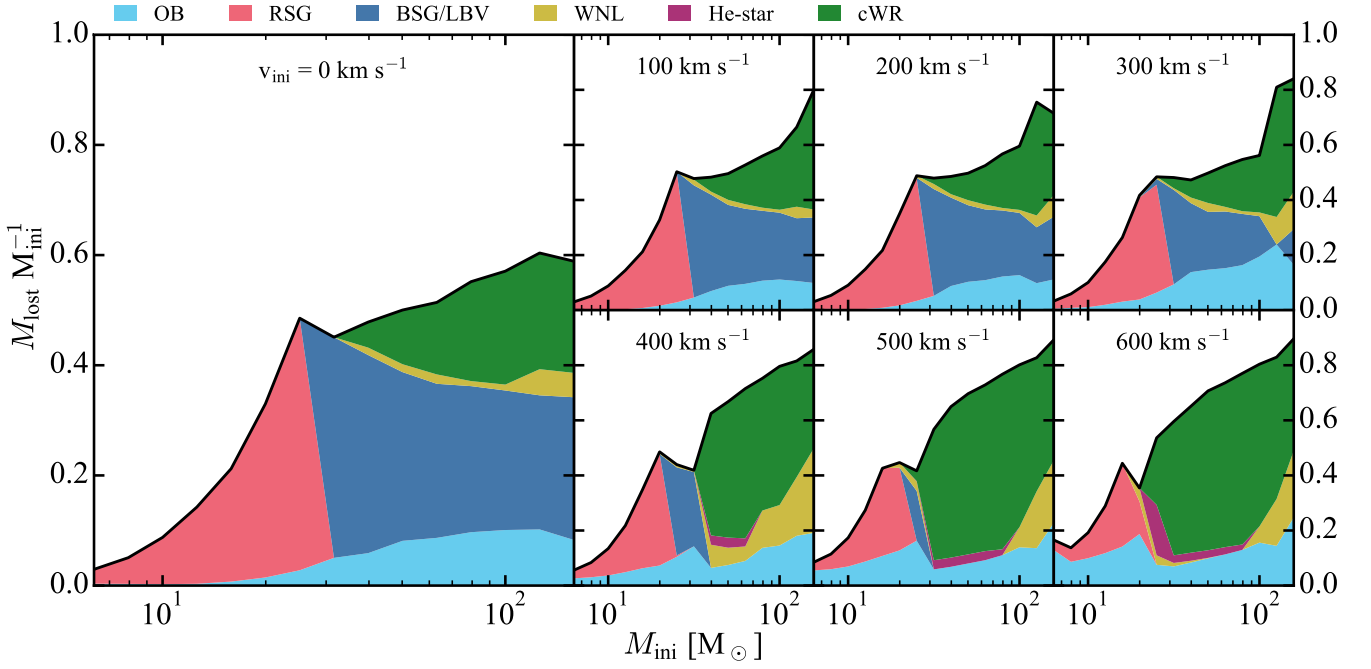


Figure A1. As in Fig. 1 but for the fractional mass-loss of single stars with $Z = 0.004$.

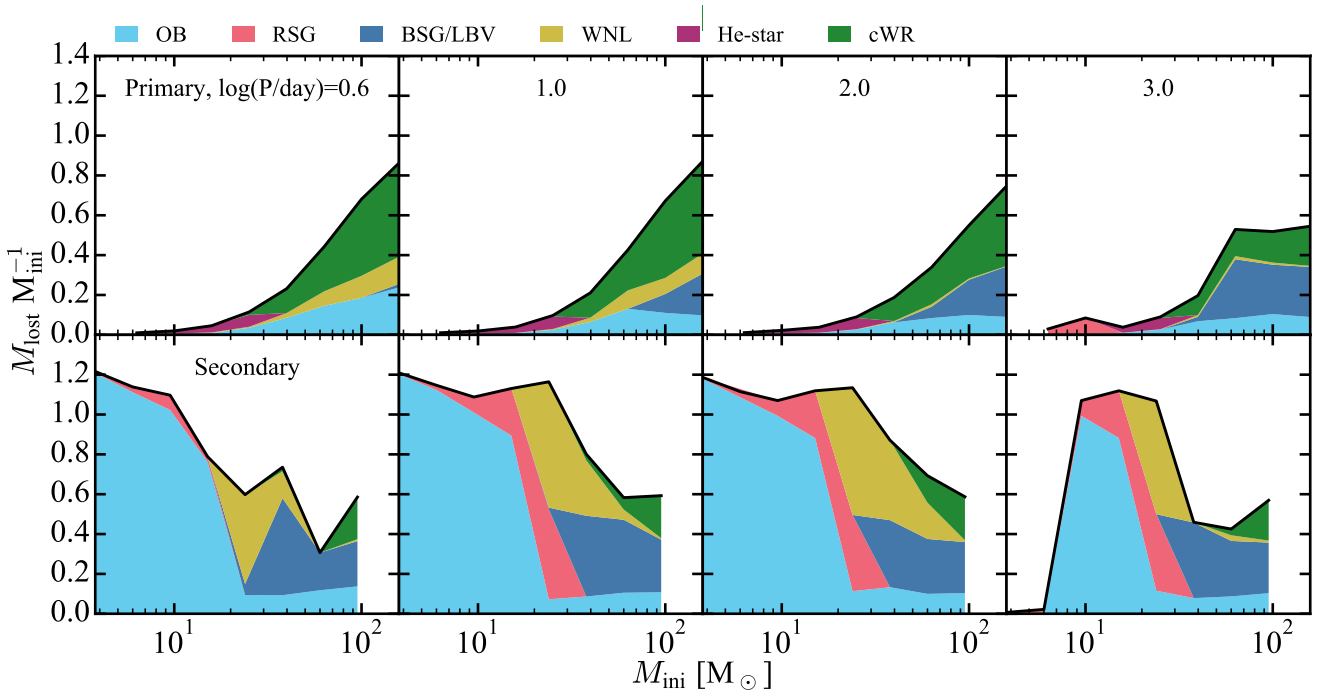


Figure A2. As in Fig. 2 but for the fractional mass-loss of binary stars with $Z = 0.004$.

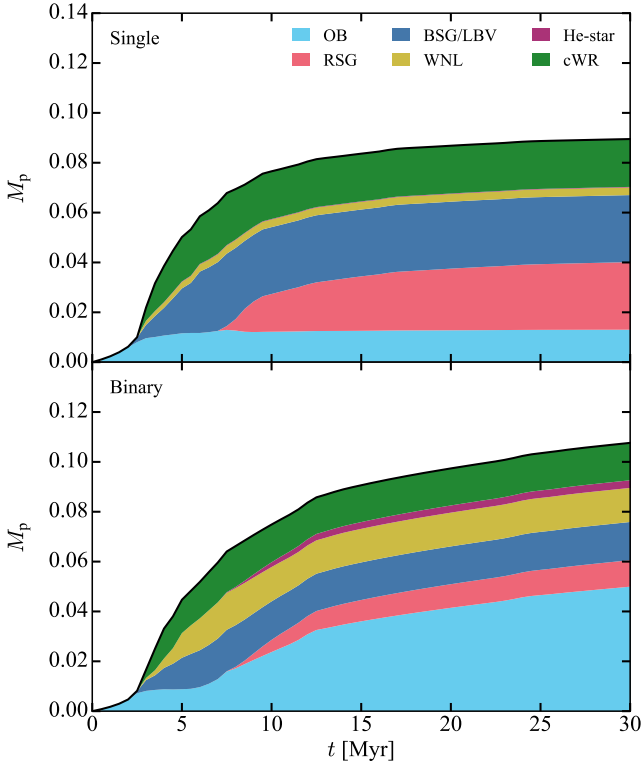


Figure A3. As in Fig. 3 but for the cumulative ejected mass in the form of winds by a coeval simple stellar population with metallicity $Z = 0.004$.

expected but the data points show substantial scatter around the regression line suggesting that other factors⁴ beyond metallicity could play a role here. One of these is environment: as it is well known that stars in high-density clusters rotate faster than those in associations while field stars have even lower average rotation velocities (Wolff et al. 2007). A large fraction of undetected binaries could also influence the results.

As a final step, we assume that $\mathcal{P}(v_{\text{ini}})$ is well approximated by a Weibull distribution. In order to determine the value of its two free parameters as a function of Z , we derive the distribution of the projected velocities following Gaige (1993) and match its median and 75th percentile to the fit we derived above. The resulting $\mathcal{P}(v_{\text{ini}})$ is then used to weigh our stellar evolutionary models and compute the feedback from a population of rotating stars.

This paper has been typeset from a $\text{\TeX}/\text{\LaTeX}$ file prepared by the author.

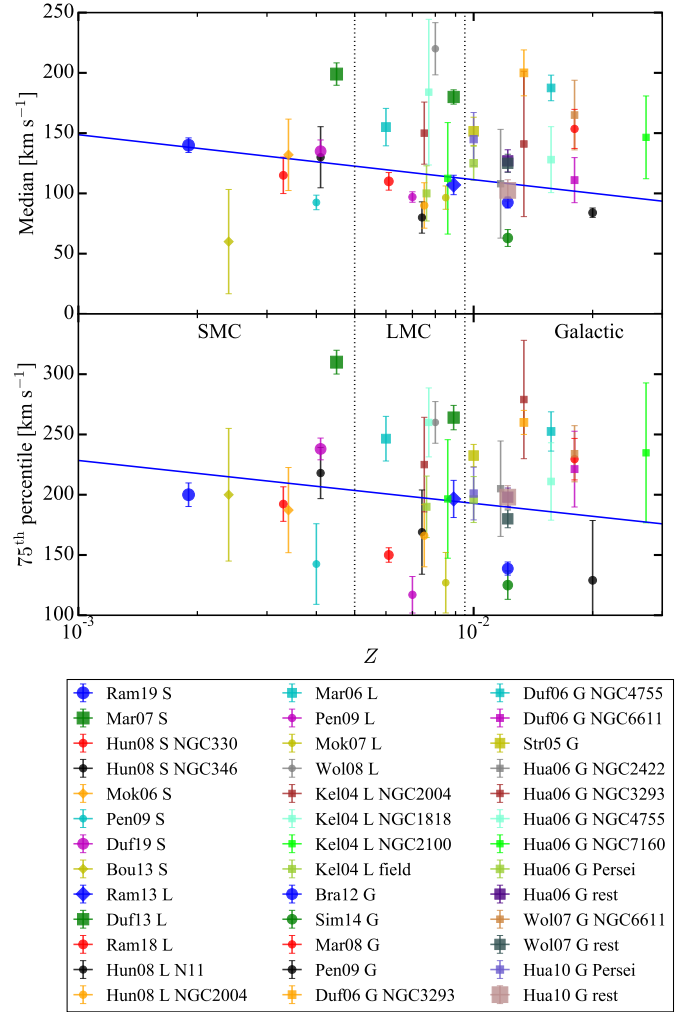


Figure B1. The median (top panel) and the 75th percentile (bottom panel) of the projected rotation velocities for different stellar clusters. The size of the symbols reflects the number of stars considered in each study while the shape of the symbols indicates the type of the stars (circles, squares and diamonds for OB, B, and O stars, respectively). The blue line shows the best-fitting relation. The dotted vertical lines separate SMC, LMC, and Galactic samples.

⁴ The method used to measure the rotation velocities might also influence the results of the different papers. However, method comparisons found small differences (e.g. 1 per cent in Dufton et al. 2013 and below 10 per cent for nearly all stars in Simón-Díaz & Herrero 2014).